9-29-2015 12:00 AM

Laminar fMRI in Auditory Cortex at 7T

Jacob JL Matthews, *The University of Western Ontario*

Supervisor: Dr. Rhodri Cusack, *The University of Western Ontario*

A thesis submitted in partial fulfillment of the requirements for the Master of Science degree in Medical Biophysics

LAMINAR FMRI IN AUDITORY CORTEX AT 7T

(Thesis format: Monograph)

by

Jacob Matthews

Graduate Program in Medical Biophysics

A thesis submitted in partial fulfillment
of the requirements for the degree of
Master of Science

The School of Graduate and Postdoctoral Studies
The University of Western Ontario
London, Ontario, Canada

Abstract

Auditory cortex is involved in the perception, attention, memory and imagery of sounds. Neuroimaging has been a rich source of information on which cortical areas are recruited for different tasks. However, a more detailed understanding has been confined to animal studies using invasive imaging modalities, and high-resolution functional descriptions of auditory cortex, including columnar/laminar specific activity, topographical organization within layers, and the way these representations transfer between processing structures remain poorly understood in humans. We present 7T fMRI as a non-invasive tool for high-resolution functional imaging of human auditory cortex on the laminar scale. We describe MATLAB tools for optimizing a segmentation pipeline in BrainVoyager, and an analysis pipeline using an SPM to examine functional differences between cortical layers of auditory cortex. These differences are measured within the context of auditory memory maintenance, imagery, and tonotopy.

Keywords

Auditory Cortex, Ultra-High-Field fMRI, Laminar, Tonotopy, Segmentation

Acknowledgments

I would first like to acknowledge my supervisor, Dr. Rhodri Cusack, for welcoming me into his lab four years ago, and offering me his guidance, wisdom, and no small amount of programming expertise ever since. The opportunities he has offered me in my time here have been enormous, and the knowledge I leave with is appreciated immensely.

I would also thank my co-supervisor, Dr. Annika Linke, for her endless advice and many hours of troubleshooting. My knowledge of everything auditory I've learned throughout my time here has stemmed from her, not to mention my healthy scientific skepticism!

Thank you to my committee members Dr. Marc Joanisse, and Dr. Ravi Menon for guiding my project with excellent suggestions, and keeping me on the rails where the scope of the project was concerned.

Thank you to Joe Gati and Trevor Szekeres at the Robarts Research Institute for their knowledge and assistance with scanner hardware and sequence decisions, and patience as we pushed the limits of their favorite scanner.

I'd like to thank members of the Cusack Lab; Laura for keeping me on task for two years and presenting me the odd programming distraction when I needed it, and Conor for having intricate physics conversations with me when I needed to talk out loud and explaining our immensely complicated analysis pipeline to me when I was lost. Thanks also to Bobby for reminding me what enthusiasm for science really looks like, Hester for reminding me how amazing I am, Charlotte for making me feel confident about where my life is headed, Leire for some of the most eye opening conversation I've ever had about the English language, Michelle for a healthy dose of flattery where my programming is concerned, and Jordynne for the delicious baked treats.

Finally I'd like to thank my better half Amanda for keeping me sane during the rough bits, encouraging me to fight off the procrastination monster, and the best warm meals I've experienced during my education, and my family, who have supported me constantly throughout everything I've ever done.

Table of Contents

List of Tables

List of Figures

List of Abbreviations

AI - Primary Auditory Cortex
AII - Secondary Auditory Cortex
BOLD - Bold Oxygenation Level Dependent [Contrast]
EPI - Echo Planar Image
fMRI - Functional Magnetic Resonance Imaging
FOV - Field of View
GE-EPI - Gradient Echo - Echo Planar Imaging
GM-CSF - Grey Matter Cerebral Spinal Fluid [Boundary]
GMG - Grey Matter Global [Threshold]
GML - Grey Matter Local [Threshold]
HG - Heschl's Gyrus
HG1 - Primary Heschl's Gyrus (split)
HG2 - Secondary Heschl's Gyrus (split)
IC - Inferior Colliculus
MGB - Medial Geniculate Body
MGBd - Dorsal Medial Geniculate Body
MGBm - Medial Medial Geniculate Body
MGBv - Ventral Medial Geniculate Body
MPRAGE - Magnetization Prepared Rapid Acquisition Gradient Echo
MRI - Magnetic Resonance Imaging
MtA - Manual to Automatic [Tool]
PSF - Point Spread Function
PT - Planum Temporale
SE-EPI - Spin Echo - Echo Planar Imaging
SNR - Signal to Noise Ratio
STG - Superior Temporal Gyrus
SWI - Susceptibility Weighted Image
V1 - Primary Visual Cortex
WM-GM - White Matter Grey Matter [Boundary]
WMG - White Matter Global [Threshold]
WML - White Matter Local [Threshold]

1 Chapter 1: Introduction

We live in a world where we're surrounded by sound. Our ability to process the sounds around us is fundamental to our interactions with the environment and other people. Our ability to communicate by speech with others is key to the human experience. But beyond speech we also depend on sound to navigate through our world, enjoy music, recognize other people, animals, or objects by the noises they make, and to predict and avoid dangers. The general pathways and processing areas of the auditory system are understood, but the method of processing at a finer level, nearer the neurons, the way our brain extracts and handles different fundamental characteristics of sound, and the process by which semantics of speech and nonverbal sounds are extracted are still being explored.

1.1 The Auditory System

Sound at its most fundamental level is a vibration conveyed through a medium, such as air, as an oscillatory pressure wave. It can be generated by any vibrating object in contact with the medium, and likewise has the potential to be received and interpreted by other objects in contact with the medium. These waveforms at their simplest can be thought of as sinusoidal waves in which amplitude corresponds to volume, frequency to pitch, and phase determines their interaction with other waves. A single of these sinusoidal waves is a pure tone with a single pitch. Most naturally occurring sounds we hear are complex waves combining many of these simple waves, creating sounds like a dog's bark or a speech sound. Humans have evolved complex auditory systems to receive and decode the many complex sounds we are exposed to on a regular basis.

This section will give an overview of the human auditory system, and motivate the elements of this system being probed by this project.

1.1.1 Auditory Pathways

Sound waves reaching the human ear vibrate the eardrum. As illustrated in Figure 1.1.1.1, the eardrum in turn conveys this vibration through a series of three tiny bones (malleus, incus, stapes) collectively known as the ossicles, which subsequently vibrate

the fluid filled inner ear via the oval window. This system allows impedance matching between the air filled outer ear and fluid filled inner ear. The fluid of the inner ear fills the cochlea, and when vibrating, causes vibrations of the basilar membrane. The basilar membrane, a stiff boundary, subsequently vibrates the organ of Corti. Hair cells on the organ of Corti are each tuned to a specific frequency, which has important consequences for the organization of the rest of the auditory system, and implications for the design of this study. They receive this vibration through stereocilia and transmit a signal via neurotransmitter release to nerve dendrites of the auditory nerve.

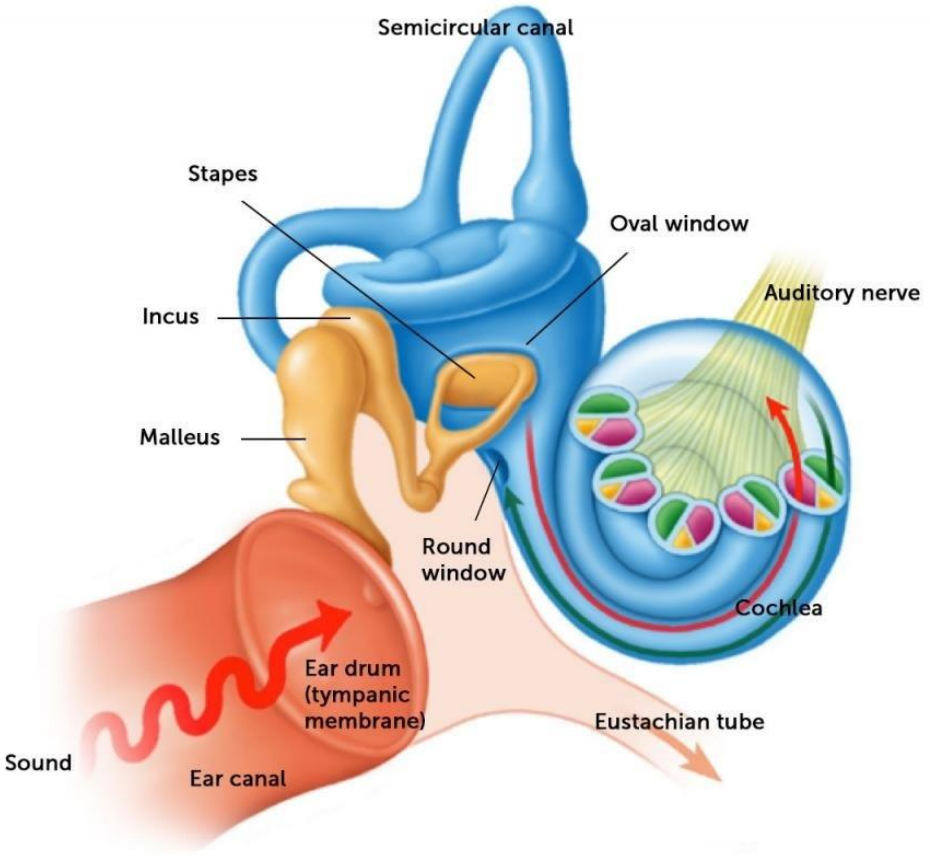

Figure 1.1.1.1 - Illustration of the structures from the ear canal to the auditory nerve. (Reused with permission from Posit Science, see 1.7 References)

Importantly for our project, the arrangement of hair cells along the length of the cochlea is in order of their preferred frequency (tonotopic). Hair cells nearest the entrance of the cochlea transduce high frequency vibrations while those towards the apex of the cochlea transduce low frequency vibrations as visualized in Figure 1.1.1.2.

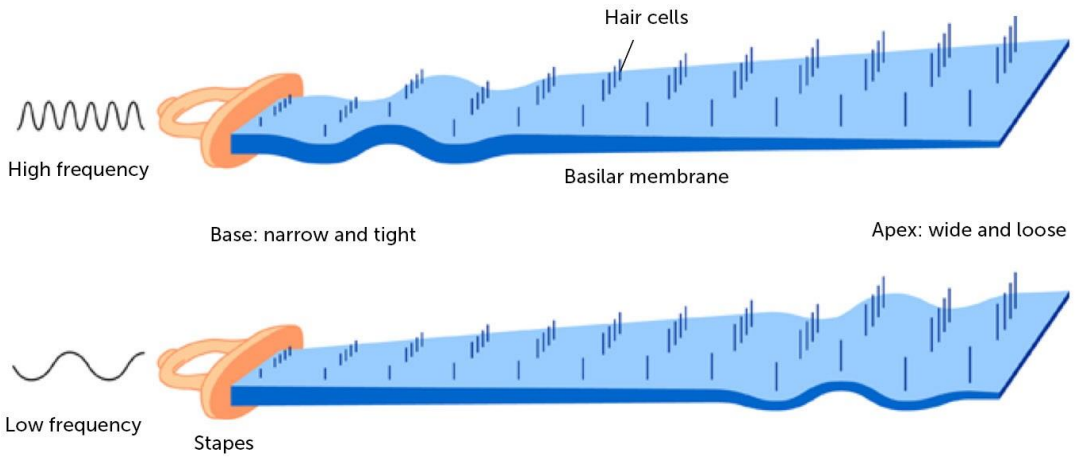

Figure 1.1.1.2 - Illustration of an unrolled basilar membrane to demonstrate the concept of tonotopy at this stage. From the base to the apex of the basilar membrane, as it bisects the cochlea, a change from narrow width and thick membrane to wide width and loose membrane occur, leading to changes in resonant frequency, and corresponding to the frequency gradient from high frequency to low frequency with which hair cells along the basilar membrane will be activated. (Reused with permission from Posit Science, see 1.7 References)

As illustrated in figure 1.1.1.3, the auditory nerve joins the vestibular nerve to form the vestibulocochlear nerve and enters the brainstem at the cochlear nuclei. From there, signals are transmitted through several subcortical structures/regions (trapezoid body, superior olivary complex, lateral lemniscus) which parcel streams into multiple parallel pathways converging in the inferior colliculus (IC) [1]. These then project to the auditory thalamus, the medial geniculate body (MGB, divided into three regions; dorsal (MGBd), ventral (MGBv), and medial (MGBm)), which has multiple connections reaching to the auditory cortex (AC), the first cortical region to process sound, and the area of study for this project.

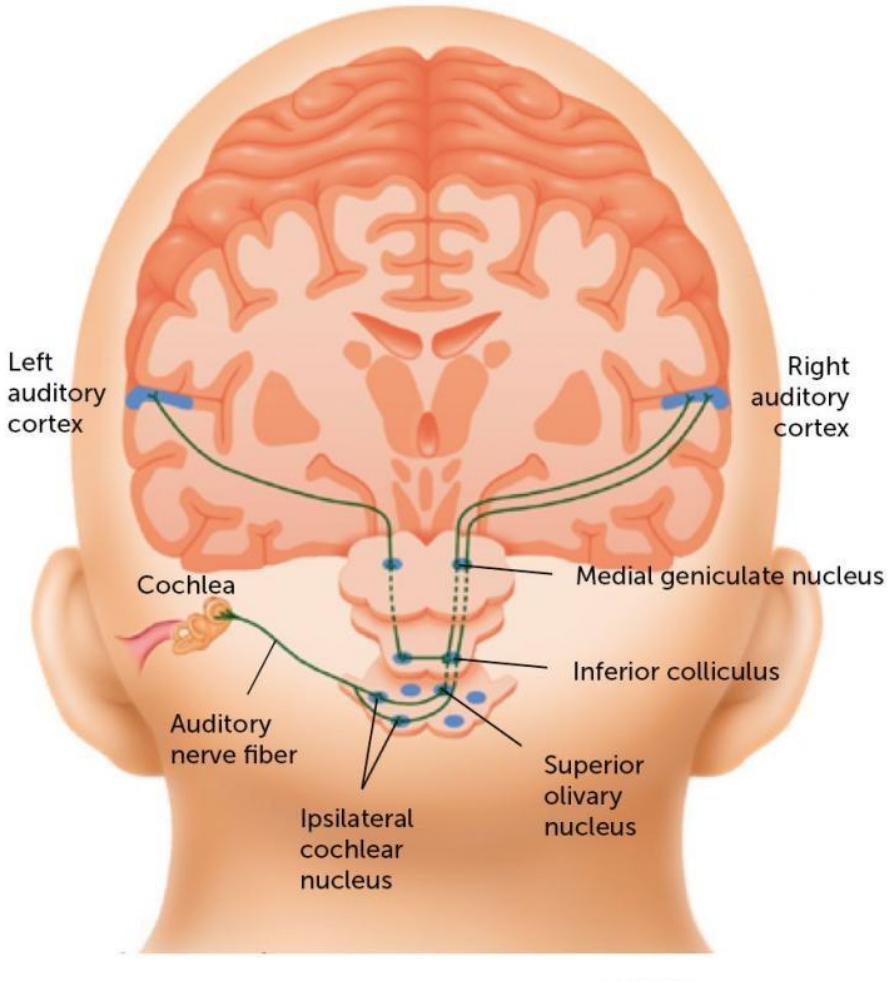

Figure 1.1.1.3 - An illustration of the auditory signal pathway originating from the auditory nerve exiting the cochlea and terminating in the auditory cortex. (Reused with permission from Posit Science, see 1.7 References)

1.1.2 Auditory Cortex and Cortical Laminae

The human auditory cortex lies within the Sylvian fissure, on the superior temporal gyrus (STG), and is broadly encompassed by Brodmann's areas (BA) 22, 41, 42, and 52. Connections from auditory cortex reach many other regions of the brain, but auditory cortex is the primary region receiving direct input from MGB. It is usually subdivided into three regions; primary auditory cortex (core region, BA41), secondary auditory cortex (belt regions, BA42), and auditory association cortex (parabelt regions, BA22 and BA52) [2]. These regions are most often determined by cytoarchitectonic

mapping, and distinguished by which regions of MGB they receive signals from. Primary auditory cortex is usually landmarked as the posterior two thirds of Heschl's Gyrus, with the secondary regions surrounding it, and the association cortex covering more anterior or lateral areas of the STG [3].

The cortical grey matter comprises six layers. In auditory cortex, these have been distinguished by cytoarchitectonic mapping, leveraging each of their characteristic distribution of neuronal cell types. The figure below from Lee, C 2013 [1] shows and describes the connections between MGB and each layer of auditory cortex.

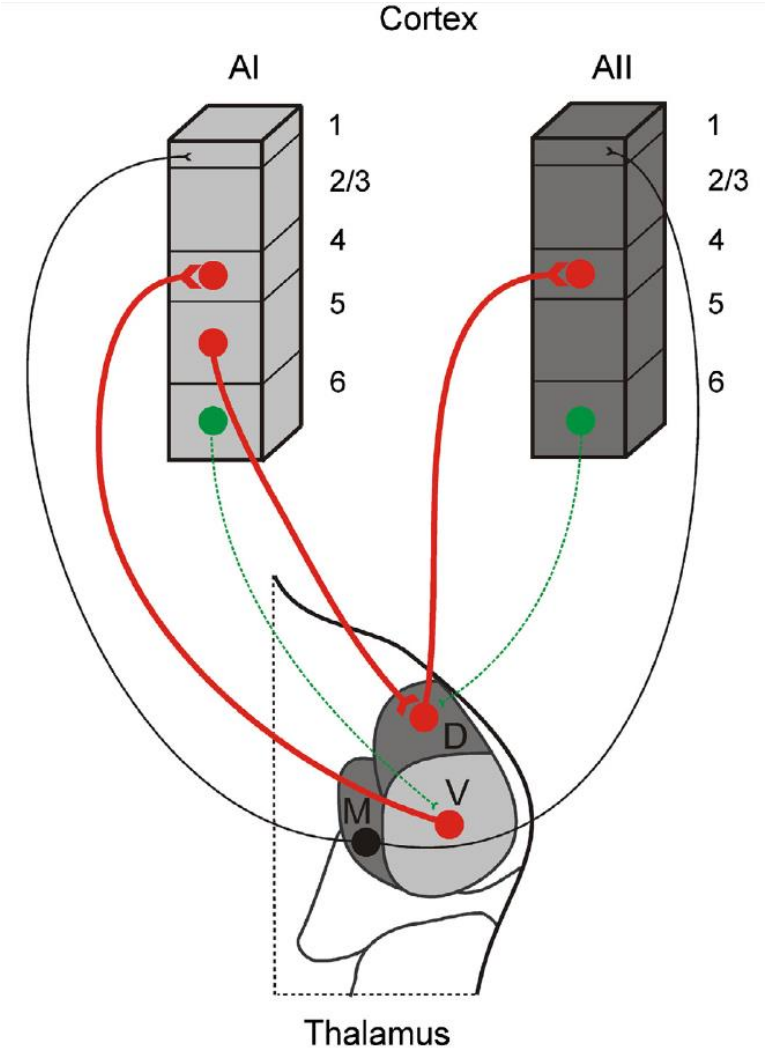

Figure 1.1.2.1 - Thalamocortical connections between MGB and AI and AII. The bulk of auditory information [4] ascends from MGBv to layer IV of AI, and MGBd to layer IV of AII (ascending red lines). Communication between AI and AII is created by feedforward

projections from layer V AI to MGBd (descending red line) [5]. Feedback circuits from layer VI of AI and AII modulates MGBv and MGBd activity respectively [6] (green lines), but is not a major conduit of information flow. Projections from MGBm connect broadly to all auditory cortex, primarily layer I [7], and are thought to potentially synchronize activity across all of auditory cortex. Light grey areas indicate regions demonstrating tonotopic organization, while dark grey are non-tonotopic. (Reused with permission from Elsevier, see 1.7 References)

The neocortex, in general, has inputs and outputs described by the below figure from Purves et al. 2004 [8]. Note that this figure is generalized across cortex, so for example, although the figure shows inputs to layer IV from both the thalamus and other cortical regions, we know that in primary auditory cortex, almost all of the layer IV input is from the thalamus, while is secondary and association auditory regions, much of the input to layer IV will be from the primary auditory cortex itself (i.e. “other cortical regions”). Note that the cortex receives input from other cortical regions to layers II and V (in certain regions of cortex, layers II and III become less distinguishable and share function [8]). These then, would be regions we expect to be more affected by top down processing feedback than layers like IV, which we would expect to mainly fluctuate with direct sensory input from the thalamus.

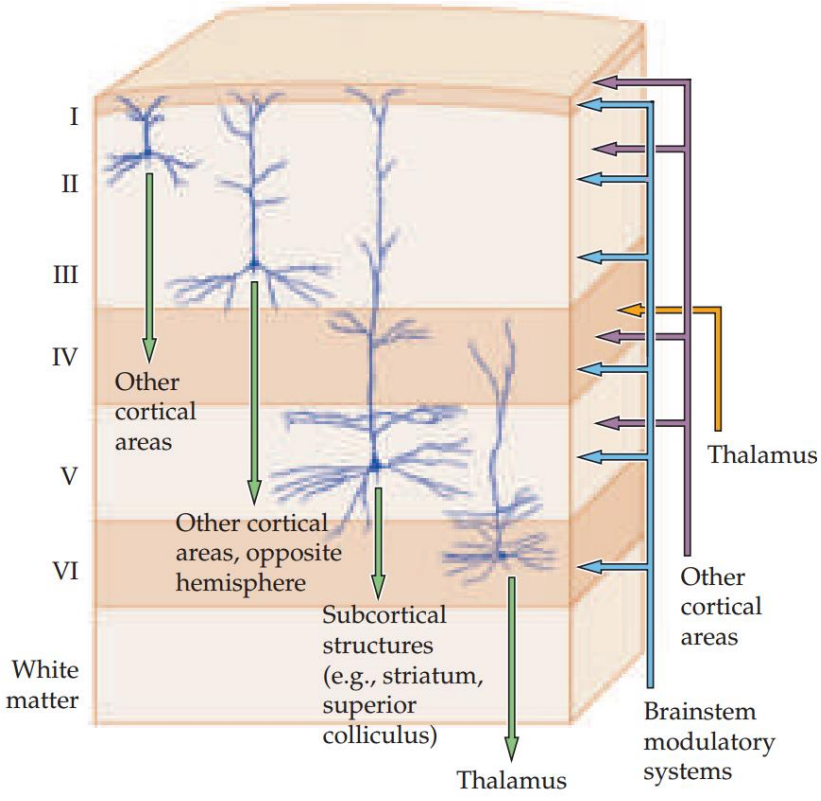

Figure 1.1.2.2 - A generalized depiction of the inputs and outputs of each layer of the neocortex. (Reused with permission from Sinauer, see 1.7 References)

1.1.3 Tonotopy

The tonotopy seen in neural tuning in the organ of Corti continues through the subcortical structures, with some tonotopy detectable even with fMRI in the human IC [9]. Tonotopic representations continue through portions of the thalamic MGB. The ventral portion of MGB receives tonotopically organized signal and projects it to layer IV primary auditory cortex (AI), while other portions deal with non-tonotopic signals. With the bulk of information transfer coming through MGBv to layer IV AI, and layer IV feeding out to other layers of AI, all layers of AI demonstrate some degree of tonotopy. Further specific findings related to tonotopy will be discussed in section 1.3, specifically the “rodents” subsection.

1.1.4 Next Steps in Understanding the Auditory System.

Important variations in neural tuning exist at fine spatial scales. Layer-specific inputs are likely to mediate function differently between layers, and topographical organization is likely to vary in turn. Visualizing these interactions will provide the next phase of understanding auditory processing in humans. In the next section, the benefits of ultra-high-fields for noninvasive imaging at fine spatial scales will be explored, before in the following section returning to a survey of the current state of the art in animal and human imaging at high resolutions, with a focus on what has been learned about auditory cortex.

1.2 Ultra High Field Imaging

The advent of ultra high field MRI (fields stronger than 3T, in our case 7T), has allowed imaging at finer resolutions while maintaining image contrast. While there are new challenges, such as decreased field homogeneity, leading to increased susceptibility artifacts and image distortion, there are particular benefits for some lines of research, such as laminar imaging. This section will briefly highlight some of the benefits of 7T MRI as they are relevant to this project.

1.2.1 Signal to Noise Ratio

At its most fundamental level, an increased B_0 field strength of an MRI will, by the Boltzmann Distribution, accentuate the difference in parallel and antiparallel spins within the field, increasing the raw signal produced by the sample. While the signal increases with the square of the field strength, signal noise also increases linearly, and so from this factor alone an approximate linear one-to-one increase in SNR would be expected. Once changes in T_1 and T_2 times are factored in, if the sequence is not modified, a doubling of field strength yields an increase in SNR of only 60-90% [10]. However, with proper application of optimal sequence design and the use of modern receive coil arrays, according to some measures it's actually found that the relation between B_0 field strength and SNR is supralinear ($SNR \sim B_0 1.65$) [11]. This benefit does not apply to all acquisitions, such as fMRI, as there are additional challenges faced in

deteriorating field homogeneity and decreasing T_2*.

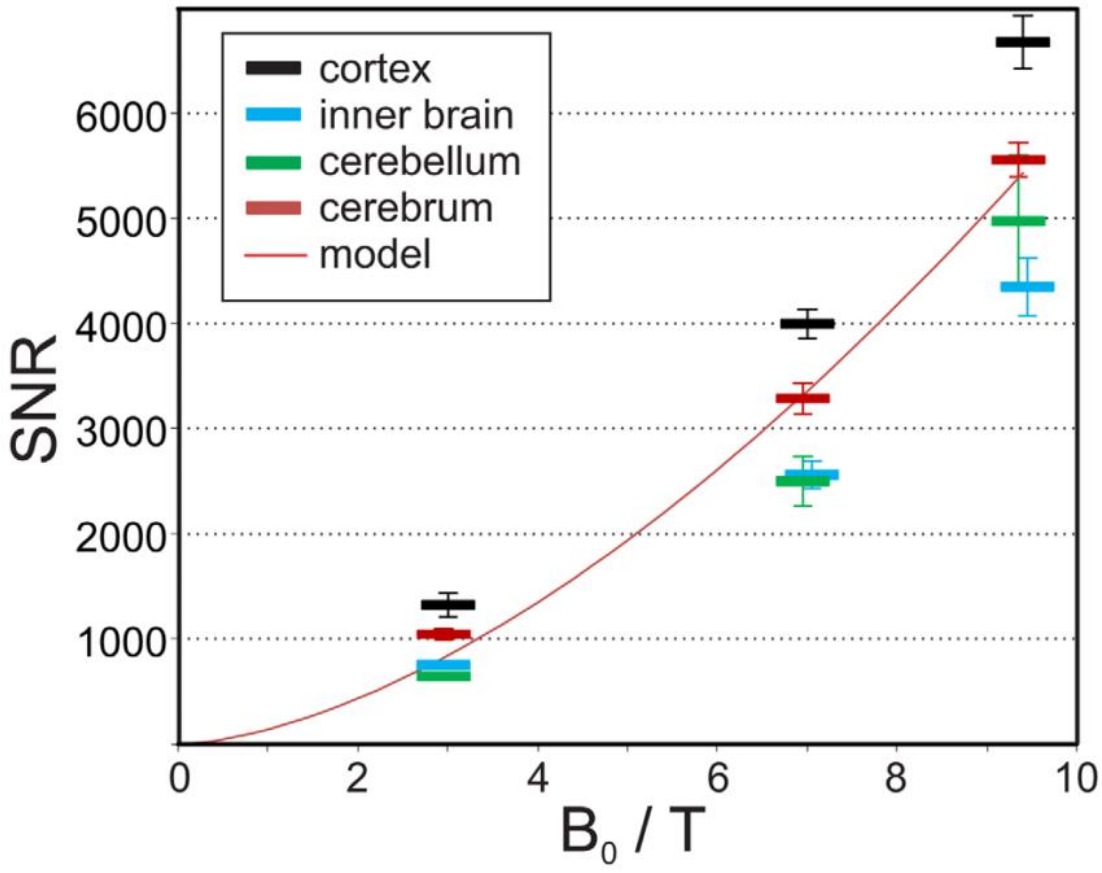

Figure 1.2.1.1 - SNR values calculated for four brain compartments at field strengths of 3T, 7T, and 9.4T. The red line is fitted to SNR values over the entire cerebrum. [11] (Reused with permission from Elsevier, see 1.7 References)

1.2.2 Functional Contrast and Image Resolution

To achieve laminar specific imaging, we require high resolution with sufficient SNR. The benefits from raw image SNR at high field also translate into temporal SNR benefits for functional imaging. The figure below from Triantafyllou et al. 2005 [12] shows the average temporal SNR (SNR of a time series of functional data) from five subjects calculated from 60 time points for a spectrum of voxel volumes at 1.5T, 3T, and 7T. The tSNR advantage at 7T is clear at all voxel volumes, growing larger at small voxel volumes.

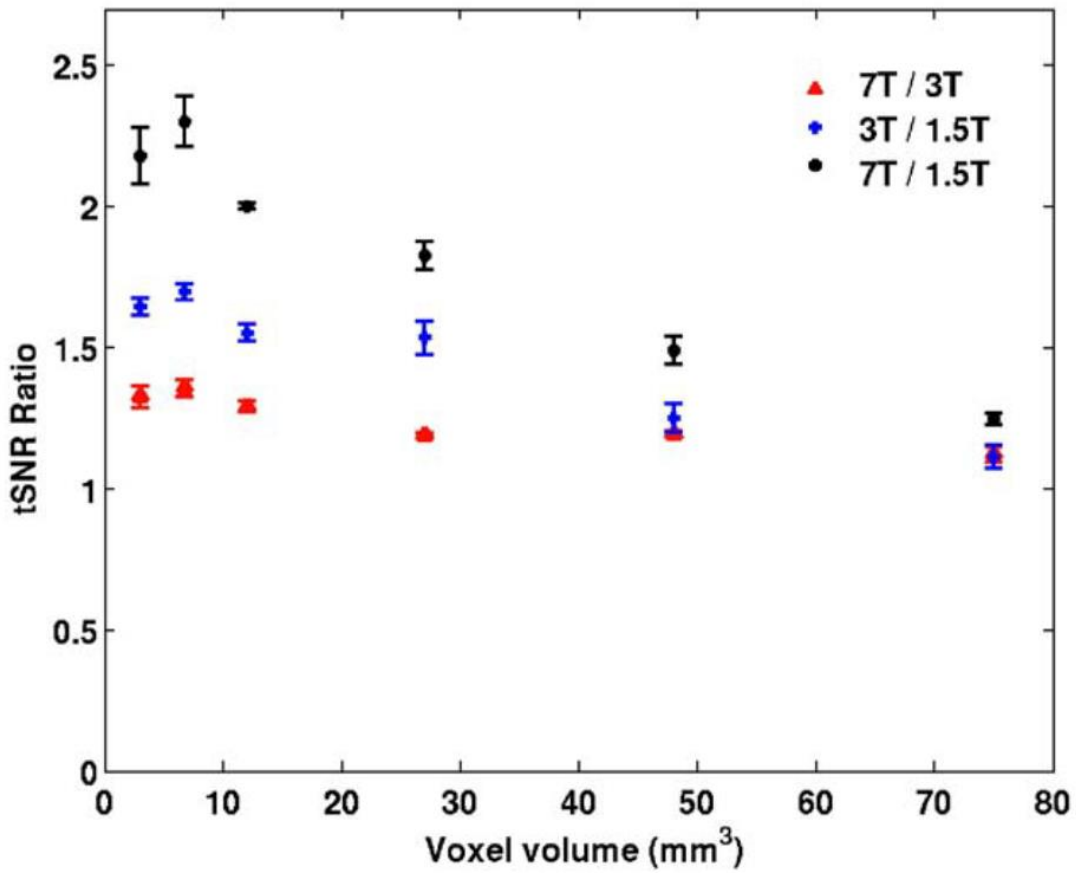

Figure 1.2.2.1 - Temporal SNR as a function of voxel volume for 1.5T, 3T, and 7T, given as ratios. [12]

Furthermore, Triantafyllou et al. distinguished the ratio of physiological "BOLD-like" noise to thermal noise by measurements with multiple TE values. The figure below from Triantafyllou et al. 2005 [12] shows the average ratio of physiological noise to thermal noise from five subjects for a spectrum of voxel volumes and TE times at 3T and 7T.

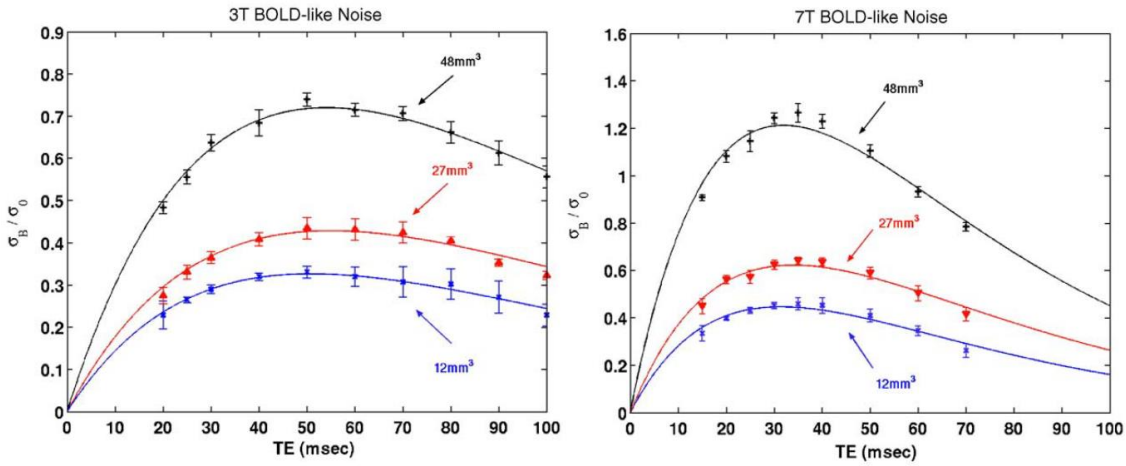

Figure 1.2.2.2 - Ratio of physiological "BOLD-like" noise to thermal noise as a function of voxel volume and TE at 3T and 7T. [12]

Triantafyllou et al. concluded that high resolution experiments in particular would benefit from 7T, and that at high resolutions when the image noise was dominated by thermal noise, exploration into RF coil design and exploitation of enhanced contrast to noise benefits would further improve upon their findings.

Additionally van der Zwaag et al. [13], expanding on work by Gati et al. [14] and Yacoub et al. [15] also found that BOLD contrast was found to increase with field strength, as well as finding evidence for reduced venous contribution to the BOLD signal at higher field strengths.

1.3 Laminar Functional Imaging

Prior to the advent of ultra-high-field MRI (>3T) it was difficult to resolve activity from different cortical layers in the human brain. This means a lot of our knowledge of functional processing at fine scales comes from work in animals utilizing invasive imaging techniques. This section summarizes work done to date studying laminar specific function, with foci on the auditory system, laminar fMRI, and human 7T fMRI.

1.3.1 Rodents

The highest resolution functional studies of auditory cortex have been in rodents. In particular recent work from Bandyopadhyay et al. [16] and Winkowski et al. [17] developed a much more detailed understanding of laminar specific activation and topography than was previously available. Several of the hypotheses of this project extend these findings from rodents to the human cortex.

Prior to the advent of sufficiently high resolution imaging modalities, many studies have used electrophysiological recording to distinguish laminar differences in AI. For example, Wallace et al. 2008 [18] used electrodes inserted orthogonally to the cortical surface in guinea pigs. They found laminar differences in frequency tuning bandwidth, response latencies, response threshold, and response to contrasted vocalizations. These were consistent with existing structural models of auditory cortex including the ordered flow of information from thalamus to particular layers of AI, descending outputs from layers V and VI, and ascending outputs from layers II and III. This study was an excellent demonstration of functional response differences between layers, but was only able to look at responses in a single column of AI, not look at differences between and across laminae.

Bandyopadhyay et al. 2010 [16] used in vivo two-photon Ca^{2+} imaging to probe for topographic organization of the mouse auditory cortex at the single cell level. This technique allowed data to be collected for neurons in patches up to 300μm^2 in size, yielding information about how specific response properties of neurons were organized across the cortex. It however, is limited to collecting data from one layer at a time, with data being collected primarily from layers II and III for this study. They were able to confirm that while tonotopy was the dominant organizational topography in primary auditory cortex and the anterior auditory field, it was present only on a broad scale across the cortex, while at small scales neighboring neurons could have substantially different characteristic response frequencies. Individual neurons also exhibited bandwidth and intensity tuning properties, but at the scale examined in this study, these were not topographically organized. Lastly, they found by examining subthreshold responses of

neurons, that it is likely that clusters of nearby neurons share input and are able to perform computations independently and in parallel using the same input.

Winkowski et al. 2013 [17] elaborated on work by Bandyopadhyay et al., by extending the use of in vivo two-photon Ca^{2+} imaging to probe for laminar differences in fine scale topographical organization of auditory cortex in mice. They used the same methods to look for the same measures in paired imaging fields in both layer II/III neurons and layer IV neurons. They find that frequency tuning is more precisely tontopically organized in layer IV, the thalamorecipient layer, than layers II/III. Clusters of neurons in layer IV showed identical or near identical best frequencies (frequencies showing the strongest response), while neurons in layers II/III in the same paired imaging field showed a greater distribution of best frequencies around the same best frequency focused on in layer IV. This pairing of medians in paired imaging fields supports the broad existence of tonotopy as an organizing topography in non-layer IV layers despite their increased heterogeneity. As well, Layer IV neurons were found to respond more strongly to tones than layer III neurons. They point to this evidence as being in line with the model of common stimulus-related input (from the thalamus) to layer IV, and a more diverse input (either from an array of thalamorecipient neurons, or intralaminar connections) to layers II/III. They conclude that between their evidence and past studies, it is suggested the representation of sound frequency in undergoing a transformation between layer IV and layers II/III.

1.3.2 Non-human Primates

Some of the earliest studies using very-high-resolution ultra-high-field fMRI to resolve laminar specific functions were completed with non-human primates. Monkeys are often the subjects for new MRI technologies, when human certified hardware technologies and SAR monitoring are not available.

Goense et al. 2006 [19] studied primary visual cortex (V1) in the macaque monkey with 4.7T MRI. Their purpose was to see if the use of spin echo EPI sequences would reduce the large vein dependence of the BOLD effect as present in gradient echo EPI sequences. All the sequences they investigated were multi-shot EPI sequences with

between 2 and 16 segments. By using the macaque monkeys as subjects, with relatively small heads, and a field of view which covered solely visual cortex, they were able to obtain images of very high spatial and temporal resolution (500μm^2 in plane resolution, 2mm slice thickness, 2 second TR). With this accuracy they were able to clearly visualize layer IV (which is very prominent in the highly ordered visual cortex) and see that the majority of their functional signal presented as distinguished peaks concentrated in layer IV and the surface layer I. They were able to further increase signal specificity in the mid layers by decreasing the readout window length, suggesting the T_2* weighting was primarily in the large veins, with T_2 weighting dominating in the capillaries. This window based benefit came at the cost of scan time. This contrasted with the GE-EPI sequence which, while showing an equivalent overall percent signal change, showed signal predominantly at the surface layers.

Goense et al. 2012 [20] continued the study of macaque V1 at 4.7T, examining laminar differences in neurovascular coupling. By measuring BOLD contrast, cerebral blood volume (CBV), and cerebral blood flow (CBF), they were able to look at laminar specificity in the relations between CBF and CBV between positive and negative BOLD responses. They found for positive BOLD responses, parallel increases in both CBV and CBF in the centre of cortex, while for negative BOLD responses CBF decreased superficially while CBV increased in the centre of cortex. The importance of these findings lay in the suggestion that there are unique neurovascular coupling mechanisms between cortical laminae, as well as between positive and negative BOLD responses.

Chen et al. 2012 [21] looked at V1 in the macaque brain at 4.7T. Using very high in-plane spatial resolution (200μm^2, 1 mm slice thickness) multi-shot (4 or 8) GE-EPI, and optimally placed FOVs derived from optical imaging, they found layer IV to be the most activated layer (30% more than superficial layers) after removing the influence of large veins. The results suggest that the point spread function (PSF) of GE-EPI is finer than previously thought, and sufficient for mapping sub-millimeter functional activity, lending itself to the study of laminar activation.

1.3.3 Humans

Studies in humans have lagged several years behind their animal counterparts and have been limited mostly to non-invasive imaging or postmortem techniques. The studies of auditory cortex similarly lag behind studies of visual cortex, which has better understood organizational principles underlying it, and less between subject anatomical variability.

Knowledge of cortical laminae in the neocortex has existed for a long time, and some of our earliest examples of functional organization (Brodmann's areas) were derived from laminar profiles of cytoarchitecture. This field has advanced with increasingly complex methods, and continues to be used to try to define functionally boundaries of cortex. There continues to be controversy on the subdivision of auditory cortex [3,22], with many arrangements of core, belt, and parabelt boundaries proposed. Chance et al. 2004 [23] studied post-mortem auditory cortex tissue samples from control and schizophrenia patients, finding thickness relationships between specific cortical laminae and gyral/sulcal combinations implicating highly localized cortical laminae in specific brain functions. The manual, and subjective nature of making decisions based on visual differentiations of microscopy images, was also recently improved upon by Schleicher et al. 2005 [24], who presented an automated, modality independent, intensity line profile based method for parcellation of the cortex. They present their method as applied to cytoarchitectural parcellation of the human auditory cortex.

Earlier studies attempted to use 3T MRI to examine laminar activity in the human brain. Ress et al. 2007 [25] used sub-millimeter imaging with custom surface receive coils and custom multi-shot sequences to successfully obtain functional activation results in human primary visual cortex (V1). This study was one of the first to prove the feasibility of laminar fMRI in humans, and the results matched expectations of laminar response profiles, thickness, and agreement between structural and functional images. Koopmans et al. 2010 [26] sacrificed temporal resolution (TR=60 seconds) in a 3D Flash sequence to achieve submillimeter resolutions with standard hardware. They found a significantly higher signal change in layer IV of human VI, and determined the GE-

BOLD contrast to have submillimeter intrinsic spatial resolution in human cortex, high enough to differentiate cortical laminae.

7T MRI allows for a higher resolution at the same signal to noise ratio (SNR), making laminar fMRI much more feasible. Polimeni et al. 2010 [27] used 1 mm isotropic single shot EPI to image human VI. They showed highly accelerated EPI limited image distortion enough to allow boundary based registration to accurately align EPI images to structurally derived surface reconstructions. They also limited selection of laminar voxels to central and deep layers to avoid the signal bias at surface layers. Olman et al. 2012 [28] used the 3D-GRASE sequence to avoid the surface vein bias of GE-EPI, and successfully characterized laminar profiles for known phenomena in human V1.

Further studies at 7T optimized the most sensitive fMRI sequence, GE-EPI BOLD, for submillimeter use in humans [29], and by investigating and optimizing less biased CBV based fMRI sequences [30], as well as comparing the less biased 3D-GRASE sequence to the 2D SE-EPI sequence [31] as well as the GE-EPI sequence [32]. Siero et al. 2014 [33] used implanted high density electrocorticography (ECoG) grids in human motor cortex in tandem with GE-EPI to assess the spatial correlation of the neuronal activity we're truly interested in to the correlate hemodynamic based BOLD contrast we measure with fMRI. It found excellent agreement in activation foci between the two modalities and successfully used both to identify a topographical layout for the movement of each finger.

Laminar fMRI imaging in auditory cortex has been very limited to date. De Martino et al. 2014 [34] used 7T MRI to localize auditory areas in the human brain. They collected structural images at 0.6mm isotropic resolutions, with T_1, T_2*, and proton density (PD) contrasts. They used a ratio T_1/PD image as an inhomogeneity reduced image for segmentation, a ratio T_2*/PD image to obtain venograms, and a ratio T_1/T_2* image to obtain an image related to local myelin content. Using segmentation-generated, depth-specific cortical laminae grids to sample from the venous masked myelin content image, they obtained column depth profiles of myelin content across auditory cortex. These profiles were submitted to a clustering algorithm to obtain parcellation of auditory

areas which they then labelled based on anatomical region, including a region with the most consistently high myelin profile in the area of Heschl's gyrus associated with AI. They validated these parcellated areas by sampling functional responses to auditory stimuli within each. They found a classic tonotopic gradient as well as more narrow frequency tuning for each subject within the area, concluding it may correspond to human AI. While the structural data were sampled by laminae, the functional data were only sampled by parcellated area, and no functional laminar results were presented.

1.4 Motivation for the Current Study

1.4.1 What's next in Laminar Auditory Imaging

Tonotopy has been found to be an important organizing principle of the auditory system in animals and humans. Work by Bandyopadhyay et al. [16] and Winkowski et al. [17] in rodents has suggested that there are laminar specific differences in tonotopy, and that this will have important implications for how auditory cortex operates. Given the many parallels between laminar architecture in rodents and humans, we expected that similar laminar specific differences in tonotopy would be seen in humans. However, their methods are invasive and cannot be used in humans. A noninvasive method of distinguishing functional responses from different layers, and ideally within layers as well, was required.

Laminar fMRI has been shown to be possible in humans, using 7T MRI, but no study to date has looked at laminar specific functional activation in auditory cortex. Furthermore, it has been shown that tonotopy can be measured in humans at 7T. We aimed to bring these together, and improve understanding the fine spatial function in human auditory cortex. The goal of this study was to address the challenges to make this possible, and evaluate the efficacy of these methods.

1.4.2 Summary of the Best Methods for Auditory Laminar fMRI

With regards to the best methods for laminar fMRI, studies to date have come to consensus on some items and not others. Ultra-high-field MRI, 7T, seems to be a requirement for laminar scale resolution, if large sacrifices are to be avoided in signal-to-

noise. While some studies performed “high resolution mapping” with resolutions coarser than 1 mm, all studies reporting “laminar specific” results utilized a 1 mm^2 in-plane resolution or higher, which seems to be a minimum for differentiating laminar effects. There is no consensus on what sequence is best for collecting functional data. Several studies have concluded that alternatives to GE-EPI such as SE-EPI and 3D GRASE have higher spatial specificity which warrants their use, while several other studies continue to use the GE-EPI sequence based on its high sensitivity and attempt to correct for its specificity issues with other methods. Nearly all studies utilize sequence acceleration, and several used reduced FOVs.

Based on these precedents, we chose to use a 7T scanner for maximized SNR at high resolutions, a GE-EPI sequence to maximize BOLD sensitivity, and a 1 mm isotropic resolution to differentiate laminar effects while still allowing coverage of one entire hemisphere.

1.4.3 Segmenting the Grey Matter

A key challenge for laminar imaging is segmenting of the anatomical boundaries of the grey matter from the cerebral spinal fluid on the superficial surface, and the white matter on the deep surface. T1-weighted images provide the highest contrast and resolution for this segmentation. However, there are then many challenges inherent in the image processing required to perform the segmentation. Chapter 3 will elaborate on these challenges, and the methods we used to address them, and to evaluate the performance of the algorithms.

1.5 Specific Goals and Framework of Thesis

The objectives of this project were:

1. Obtain high resolution structural and functional data in auditory cortex at 7T.
2. Create an optimized segmentation pipeline for specifying the locations of cortical laminae by depth.
3. Create a pipeline for analysing the functional data as a function of cortical depth.
4. Identify differences in functional activation at varying cortical depths.

1.6 References

1. Lee, C. C. (2013). Thalamic and cortical pathways supporting auditory processing. Brain and Language, 126(1), 22–28. doi:10.1016/j.bandl.2012.05.004
2. Hackett, T. a. (2014). Anatomical organization of the auditory cortex. Journal of the American Academy of Audiology, 19(10), 774–779. doi:10.3766/jaaa.19.10.5
3. Wallace, M. N., Johnston, P. W., & Palmer, A. R. (2002). Histochemical identification of cortical areas in the auditory region of the human brain. Experimental Brain Research. Experimentelle Hirnforschung. Expérimentation Cérébrale, 143(4), 499–508. doi:10.1007/s00221-002-1014-z
4. Hackett, T. a. (2011). Information flow in the auditory cortical network. Hearing Research, 271(1-2), 133–146. doi:10.1016/j.heares.2010.01.011
5. Sherman, S. M., & Guillery, R. W. (2006). Exploring the thalamus. San Diego Academic Press. Retrieved from http://books.google.com/books/about/Exploring_the_thalamus.html?id=L7WAeCvWJ04C
6. Llano, D. A., & Sherman, S. M. (2008). Evidence for nonreciprocal organization of the mouse auditory thalamocortical-corticothalamic projection systems. Journal of Comparative Neurology, 507(2), 1209–1227.
7. Hashikawa, T., Rausell, E., Molinari, M., & Jones, E. G. (1991). Parvalbumin- and calbindin-containing neurons in the monkey medial geniculate complex: Differential distribution and cortical layer specific projections. Brain Research, 544(2), 335–341. doi:10.1016/0006-8993(91)90076-8
8. Purves, D. (2004). Neuroscience Third Edition. Vascular (Vol. 3). doi:978-0878937257
9. Ress, D., & Chandrasekaran, B. (2013). Tonotopic organization in the depth of human inferior colliculus. Frontiers in Human Neuroscience, 7(September), 586. doi:10.3389/fnhum.2013.00586
10. Merkle, E. M., & Dale, B. M. (2006). Abdominal MRI at 3.0 T: the basics revisited. AJR. American Journal of Roentgenology, 186(6), 1524–1532. doi:10.2214/AJR.05.0932

11. Pohmann, R., Speck, O., & Scheffler, K. (2015). Signal-to-Noise Ratio and MR Tissue Parameters in Human Brain Imaging at 3, 7, and 9.4 Tesla Using Current Receive Coil Arrays, 00, 1–9. doi:10.1002/mrm.25677
12. Triantafyllou, C., Hoge, R. D., Krueger, G., Wiggins, C. J., Potthast, a., Wiggins, G. C., & Wald, L. L. (2005). Comparison of physiological noise at 1.5 T, 3 T and 7 T and optimization of fMRI acquisition parameters. NeuroImage, 26(1), 243–250. doi:10.1016/j.neuroimage.2005.01.007
13. Van der Zwaag, W., Francis, S., Head, K., Peters, A., Gowland, P., Morris, P., & Bowtell, R. (2009). fMRI at 1.5, 3 and 7 T: characterising BOLD signal changes. NeuroImage, 47(4), 1425–34. doi:10.1016/j.neuroimage.2009.05.015
14. Gati, J. S., Menon, R. S., Uğurbil, K., & Rutt, B. K. (1997). Experimental determination of the BOLD field strength dependence in vessels and tissue. Magnetic Resonance in Medicine, 38(2), 296–302. doi:10.1002/mrm.1910380220
15. Yacoub, E., Shmuel, a, Pfeuffer, J., Van De Moortele, P. F., Adriany, G., Andersen, P., Hu, X. (2001). Imaging brain function in humans at 7 Tesla. Magnetic Resonance in Medicine, 45(4), 588–94. doi:10.1002/mrm.1080
16. Bandyopadhyay, S., Shamma, S. a, & Kanold, P. O. (2010). Dichotomy of functional organization in the mouse auditory cortex. Nature Neuroscience, 13(3), 361–8. doi:10.1038/nn.2490
17. Winkowski, D. E., & Kanold, P. O. (2013). Laminar transformation of frequency organization in auditory cortex. The Journal of Neuroscience: The Official Journal of the Society for Neuroscience, 33(4), 1498–508. doi:10.1523/JNEUROSCI.3101-12.2013
18. Wallace, M. N., & Palmer, a R. (2008). Laminar differences in the response properties of cells in the primary auditory cortex. Experimental Brain Research. Experimentelle Hirnforschung. Expérimentation Cérébrale, 184(2), 179–91. doi:10.1007/s00221-007-1092-z
19. Goense, J. B. M., & Logothetis, N. K. (2006). Laminar specificity in monkey V1 using high-resolution SE-fMRI. Magnetic Resonance Imaging, 24(4), 381–92. doi:10.1016/j.mri.2005.12.032

20. Goense, J., Merkle, H., & Logothetis, N. K. (2012). Article High-Resolution fMRI Reveals Laminar Differences in Neurovascular Coupling between Positive and Negative BOLD Responses, 629–639.
21. Chen, G., Wang, F., Gore, J. C., & Roe, A. W. (2012). Layer-specific BOLD activation in awake monkey V1 revealed by ultra-high spatial resolution functional magnetic resonance imaging. NeuroImage, 1–9. doi:10.1016/j.neuroimage.2012.08.060
22. Morosan, P., Rademacher, J., Schleicher, A., Amunts, K., Schormann, T., & Zilles, K. (2001). Human primary auditory cortex: cytoarchitectonic subdivisions and mapping into a spatial reference system. NeuroImage, 13(4), 684–701. doi:10.1006/nimg.2000.0715
23. Chance, S. a, Tzotzoli, P. M., Vitelli, A., Esiri, M. M., & Crow, T. J. (2004). The cytoarchitecture of sulcal folding in Heschl's sulcus and the temporal cortex in the normal brain and schizophrenia: lamina thickness and cell density. Neuroscience Letters, 367(3), 384–8. doi:10.1016/j.neulet.2004.06.041
24. Schleicher, a, Palomero-Gallagher, N., Morosan, P., Eickhoff, S. B., Kowalski, T., de Vos, K., Zilles, K. (2005). Quantitative architectural analysis: a new approach to cortical mapping. Anatomy and Embryology, 210(5-6), 373–86. doi:10.1007/s00429-005-0028-2
25. Ress, D., Glover, G. H., Liu, J., & Wandell, B. (2007). Laminar profiles of functional activity in the human brain. NeuroImage, 34(1), 74–84. doi:10.1016/j.neuroimage.2006.08.020
26. Koopmans, P. J., Barth, M., & Norris, D. G. (2010). Layer-specific BOLD activation in human V1. Human Brain Mapping, 31(9), 1297–304. doi:10.1002/hbm.20936
27. Polimeni, J. R., Fischl, B., Greve, D. N., & Wald, L. L. (2010). Laminar analysis of 7T BOLD using an imposed spatial activation pattern in human V1. NeuroImage, 52(4), 1334–1346. doi:10.1016/j.neuroimage.2010.05.005
28. Olman, C. a, Harel, N., Feinberg, D. a, He, S., Zhang, P., Ugurbil, K., & Yacoub, E. (2012). Layer-specific fMRI reflects different neuronal computations at

different depths in human V1. PloS One, 7(3), e32536. doi:10.1371/journal.pone.0032536

29. Heidemann, R. M., Ivanov, D., Trampel, R., Fasano, F., Meyer, H., Pfeuffer, J., & Turner, R. (2012). Isotropic submillimeter fMRI in the human brain at 7 T: Combining reduced field-of-view imaging and partially parallel acquisitions. Magnetic Resonance in Medicine : Official Journal of the Society of Magnetic Resonance in Medicine / Society of Magnetic Resonance in Medicine, im, 1–11. doi:10.1002/mrm.24156
30. Huber, L., Goense, J., Kennerley, A. J., Trampel, R., Guidi, M., Reimer, E., Möller, H. E. (2014). Cortical lamina-dependent blood volume changes in human brain at 7T. NeuroImage, 107, 23–33. doi:10.1016/j.neuroimage.2014.11.046
31. Kemper, V. G., De Martino, F., Vu, A. T., Poser, B. a., Feinberg, D. a., Goebel, R., & Yacoub, E. (2015). Sub-millimeter T2 weighted fMRI at 7 T: comparison of 3D-GRASE and 2D SE-EPI. Frontiers in Neuroscience, 9(May), 1–14. doi:10.3389/fnins.2015.00163
32. De Martino, F., Zimmermann, J., Muckli, L., Ugurbil, K., Yacoub, E., & Goebel, R. (2013). Cortical depth dependent functional responses in humans at 7T: improved specificity with 3D GRASE. PloS One, 8(3), e60514. doi:10.1371/journal.pone.0060514
33. Siero, J. C. W., Hermes, D., Hoogduin, H., Luijten, P. R., Ramsey, N. F., & Petridou, N. (2014). BOLD matches neuronal activity at the mm scale: A combined 7T fMRI and ECoG study in human sensorimotor cortex. NeuroImage, 101, 177–184. doi:10.1016/j.neuroimage.2014.07.002
34. De Martino, F., Moerel, M., Xu, J., van de Moortele, P.-F., Ugurbil, K., Goebel, R., Formisano, E. (2014). High-Resolution Mapping of Myeloarchitecture In Vivo: Localization of Auditory Areas in the Human Brain. Cerebral Cortex (New York, N.Y.: 1991). doi:10.1093/cercor/bhu150

Figure 1.1.1.1, 1.1.1.2, 1.1.1.3 - Reprinted from http://www.brainhq.com/brain-resources/image-gallery/auditory-images with permission from Posit Science.

Figure 1.1.2.1 - Reprinted from Brain and Language, Volume 126, Charles C. Lee, Thalamic and cortical pathways supporting auditory processing., Pages 22-28, 2013, with permission from Elsevier.

Figure 1.1.2.2 – Reprinted from Neuroscience Third Edition, Purves et al. 2004, with permission from Sinauer.

Figure 1.2.1.1 - Reprinted from Magnetic Resonance in Medicine, Pohmann, R., Speck, O. and Scheffler, K., Signal-to-Noise Ratio and MR Tissue Parameters in Human Brain Imaging at 3 , 7 , and 9.4 Tesla Using Current Receive Coil Arrays., 2015, with permission from Elsevier.

Figure 1.2.2.1, 1.2.2.2 - Reprinted from NeuroImage, Triantafyllou, C., Hoge, R. and Krueger, G., Wiggins, C.J., Potthast, A., Wald, L.L., Comparison of physiological noise at 1.5 T, 3 T and 7 T and optimization of fMRI acquisition parameters., 2005, with permission from Elsevier.

2 Chapter 2: Protocols

This chapter will cover image acquisition parameters and the motivations behind their choice, and the experiment design.

2.1 Scanner

All of the images for this experiment were acquired on a Varian/Agilent 7T 680 actively shielded, horizontal bore, human neuro system with a Siemens AC84 head coil operating at SR350. The system was equipped with 16 independent RF transmitters and 32 receivers, and imaging was done with a 16 channel Tx, 31 channel Rx head coil.

2.2 Structural Images

The requirements for our structural scans were sufficient resolution to reduce partial volume effects (discussed in 3.1.3), and strong enough tissue contrast to provide cleanly delineable boundaries between white and grey matter. Further discussion of segmentation requirements occurs in section 3.1.

2.2.1 Resolution

As localization of the cortical sheet was critical to this project, it was decided to devote an entire scanning session to structural imaging, so that multiple averages of a high resolution protocol could be used to obtain sufficient signal-to-noise. Based on pilot work by Joe Gati at the Centre for Functional and Metabolic Mapping, a protocol was selected that balanced resolution and signal-to-noise, with 0.6 mm isotropic voxels.

2.2.2 Acquisition Parameters

Structural images were acquired with a T_1-weighted 3D magnetization-prepared rapid acquisition gradient echo (3D-MPRAGE) sequence (FOV = 150x220x172mm, matrix = 250x366x286 voxels, voxel size = 0.6x0.6x0.6mm, Grappa = 2x2, TE = 2.75ms, TR = 8.88ms, TI = 1200ms, flip angle = 11 degrees).

2.3 Functional Images

The requirements for our functional scans were a sufficiently high resolution to distinguish BOLD signal from varying depths of the cortical grey matter, and a sufficiently short repetition time (TR) to reliably model changes in brain activity between different phases of our tasks.

2.3.1 Functional Resolution

The resolution required for laminar functional imaging was discussed in section 1.3 and summarized in 1.4.2. Our goal was a resolution of 1 mm isotropic or higher. In pilot work, we found scans of over 10 minutes could be acquired at 1 mm isotropic resolutions without problems. Due to limitations of the scanner gradient cooling, attempts to scan at higher resolutions (0.75 mm isotropic) were met with unpredictable maximum scan termination at times as short as 2 minutes. Thus, 1 mm isotropic resolution was chosen.

2.3.2 Other parameters

To resolve brain responses to the different phases of our task, we chose TR=2 s, as this has been shown to be effective in similar previous studies [1,2]. This and the resolution constrained the field-of-view (FOV), parallel acceleration, and other optimizations. With advice from Joe Gati, we used a GRAPPA parallel acceleration factor of 3 and a ¾ fractional k-space. This still restricted the FOV, and whole brain coverage was not possible. As a compromise, we chose to just acquire a single hemisphere, with 34 sagittal slices.

2.3.3 B_1 Shimming

Shimming in general refers to the process of increasing the homogeneity of the magnetic field inside the scanner by manipulation of the various coils. Active B_1 shimming involves adjusting the current passing through each channel of multi-channel transmit coil to achieve optimal homogeneity in the transmitted field. Manual B1 field shimming was applied before image acquisitions each session. Manual shimming presents a challenge, as the resulting field will be slightly different each scanning session,

but allows for a particular focus to be made in the process. Because of the single hemisphere FOV used, manual shimming allowed for the field homogeneity to be maximized over just one hemisphere without worrying about the surrounding tissues.

2.3.4 Acquisition Parameters

Functional images were acquired with a T_2*-weighted gradient-echo echo planar imaging (GE-EPI) sequence (34 Slices, FOV = 192x96mm, Matrix = 192x96 voxels, voxel size = 1x1x1 mm, Grappa = 2, TE = 20ms, TR = 2000ms, flip angle = 60 degrees).

Also acquired were even higher resolution GE-EPI images (30 Slices, FOV = 96x192mm, Matrix = 128x256 voxels, voxel size = 0.75x0.75x0.75mm, Grappa = 3, ¾ fractional k-space TE = 23.61ms, TR = 2000ms, flip angle = 60 degrees).

2.4 Field Maps

2.4.1 EPI Distortion

EPI spatial distortion is an artifact inherent to the EPI sequence. The EPI sequence (all of its variations) utilizes a single excitation RF pulse, and then a train of signal echo collection, allowing an entire k-space plane to be collected in tens of milliseconds (and a whole brain volume to be acquired in seconds). However, because signal is being received so long after the excitation pulse (most sequences acquire only one echo immediately following the excitation pulse) the image reconstruction is more susceptible to field inhomogeneities. This manifests as nonlinear compressions and extensions of spatial location along the phase encode dimension of the image. While there are several methods of reducing this artifact by fine tuning the EPI sequence, they are usually at odds with the sensitivity to the BOLD signal, meaning retrospective correction is often required. One popular method of retrospective correction involves acquiring field map images, which measure the voxelwise field strength, and can allow for the calculation of expected spatial distortion at each voxel.

2.4.2 Acquisition Parameters

Field Maps were collected with the following parameters (FOV = 200x180x180mm, matrix = 64x64x48 voxels, TR = 8ms, TE1 = 0.75ms, echo spacing = 0.92ms, echo increment = 0.2ms, number of echoes = 5).

2.5 Experiment Design

The goal of our experiment was to probe for laminar specificity and tonotopic representations in auditory processing. To that end we presented a series of pure tone auditory stimuli with two tasks (change detection and imagery) to probe for laminar specificity, and two conditions (high and low frequencies) to probe for tonotopy. This section will break down the details of the auditory stimuli and the experiments design.

2.5.1 Stimulus Details

Stimuli for the experiment were short pure tone melodies. Each melody was comprised of a series of 6 pure tones. The tones were always one of three tones from two frequency ranges, specifically 0, 1 or 2 semitones above the note A4 (440 Hz, 466 Hz, and 494 Hz) for the “low range”, and one octave higher (880 Hz, 932 Hz, and 988 Hz) for the “high range”. Thus a melody consisted of the three tones from one of these ranges repeated twice each in a random order. Each tone was 0.4 seconds long with sound gaps of 0.12 seconds for melodies that were 3 seconds long in total. These frequencies were intended to evoke a clear tonotopic distinction between the low and high ranges.

2.5.2 Design Details

Participants performed two different tasks while in the scanner; a change detection task and an imagery task. In both tasks, sounds were presented using Matlab with Psychtoolbox [3] and played through Sensimetrics MRI compatible in-ear headphones at a comfortable listening volume.

During the change detection task, one melody was played followed by a silent maintenance/delay period. Participants then heard the same melody again. In 50% of the trials, one tone within the melody was changed. Participants were instructed to respond as

soon as the second sound had finished playing by pressing one of two buttons to indicate a “same” or “different” response. The maintenance period and the intertrial interval (ITI) were jittered (4-11 sec) to ensure that the different phases of the task could be modeled separately in the fMRI analysis.

During the imagery task, participants again heard one melody during the encoding period. Like in the change detection task, the following delay period was jittered (4–11 sec) and participants were instructed to imagine, as vividly as possible, the melody they had just heard, repeating it in their head for the duration of the delay. Participants then heard the same melody again. Participants were instructed to respond as soon as the second sound had finished playing by pressing one of two buttons to indicate a “vivid” or “weak” response depending on how well their imagined melody matched the second playing. Like for the change detection task, the response phase was followed by a variable ITI (4–11 sec).

Each block, for both tasks, consisted of 6 subblocks with 4 trials each and took approximately 8.6 min. Each of 4 delay/ITI jitter times (4, 6.33, 8.66, and 11 seconds) was presented once per subblock. Similarly, two melodies from each frequency range were played in each subblock in a randomized order. The particular melodies presented during the encoding period of each trial were randomized.

2.5.3 Participant Details and Scanning Sessions

It was decided to focus on a proof-of-principle, by acquiring a large quantity of data in a single volunteer. One healthy female participant, age 23, took part in the experiment as a paid volunteer. She reported normal hearing and had no intensive musical training or perfect pitch. She completed a session of structural scans, and sixteen blocks of functional scans over five sessions. One other participant completed the task previously using older scanning sequences and hardware, and a second participant was scanned for structural images only; thus neither of their data were used in the final pipeline. Ethical approval was obtained from the Western University Health Sciences Research Ethics Board and subjects gave informed, written consent prior to participating.

2.6 References

1. Linke, A. C., Vicente-Grabovetsky, A., & Cusack, R. (2011). Stimulus-specific suppression preserves information in auditory short-term memory. Proceedings of the National Academy of Sciences of the United States of America, 2–7. doi:10.1073/pnas.1102118108
2. Linke, A. C., & Cusack, R. (2015). Flexible information coding in human auditory cortex during perception, imagery, and STM of complex sounds. Journal of Cognitive Neuroscience, 7(27), 1322–1333. doi:10.1162/jocn_a_00780
3. Brainard, D. H. (1997). The Psychophysics Toolbox. *Spatial Vision*, *10*(4), 433–436.

3 Chapter 3: Segmentation

A core challenge of this project lay in segmenting the cortical sheet in the structural images. Without accurate segmentation the location and cortical depth specificity would be unattainable. This chapter covers the underlying challenges facing MRI segmentation, the tools available for use, the pipeline used in this project, the optimization of the pipeline for our data, and evaluations of the resulting accuracy estimates of the segmentation.

3.1 Complications in MRI Segmentation

The challenge inherent in image segmentation in any modality usually boils down to several sources of noise. In MRI images these are usually categorized into three difficulties [1]; Image noise (machine or physiological contributions), the bias field (low frequency signal variation across the tissue stemming from field inhomogeneity), and the partial volume effect (multiple tissue types being sampled for a single voxel signal). This section will briefly address these with relation to this project's structural image segmentation, as well as the additional challenges faced using the resulting segmentation data in conjunction with functional scans.

3.1.1 Signal Noise

As in any imaging modality, MRI is subject to noise polluting the real signal being measured. Some of this noise is inherent to the scanner; electronic interference due to thermal constraints or inductive coupling between receive coils. This is usually considered to be random noise of a Rician (or Gaussian at high SNR) distribution [2]. Several methods of "de-noising" exist [1], but most make a compromise between having noise in the image and losing detailed features in the image. Other noise comes from physiological sources; fluctuations in metabolic linked brain physiology, and blood pressure fluctuations in large arteries [3]. This noise is non-random and affects certain brain structures more than others. Physiological noise predominantly affects low TR image sequences used in functional MRI and less so the long TR structural sequences due to the relatively high frequency of physiological processes.

This study used multiple scan averaging to deal with noise in the structural images. By collecting multiple structural scans, aligning them to one another, and averaging them together, the contribution of noise is reduced, and SNR is increased approximately by a factor of N, where N is the number of averaged scans. The below figures show a single scan, and an average of four scans, both after brain extraction and bias field removal. Figures after this section will depict the four scan average structural unless noted otherwise.

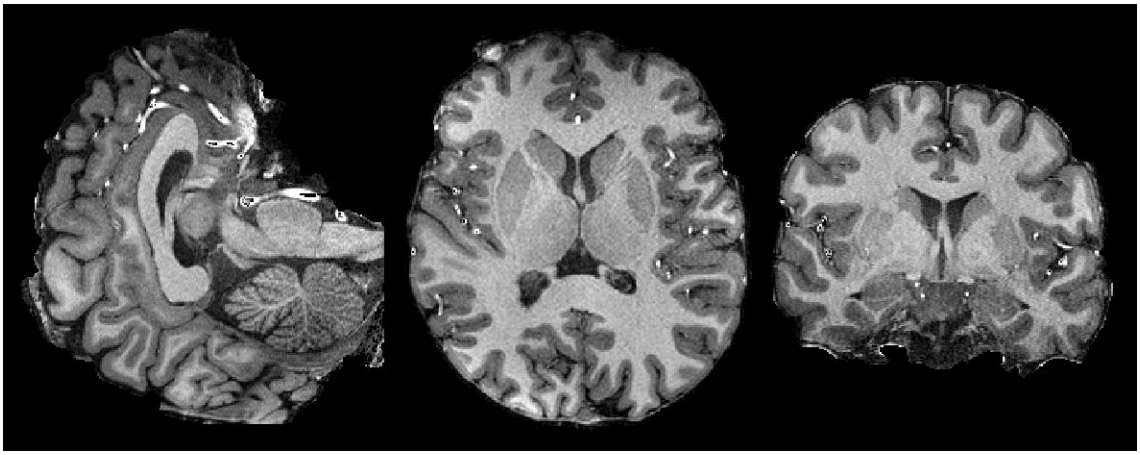

Figure 3.1.1.1 - Slices through a single scan structural image. Noise in the image is evident in the grainy texture of the homogeneous regions, and the blurred boundaries in some regions.

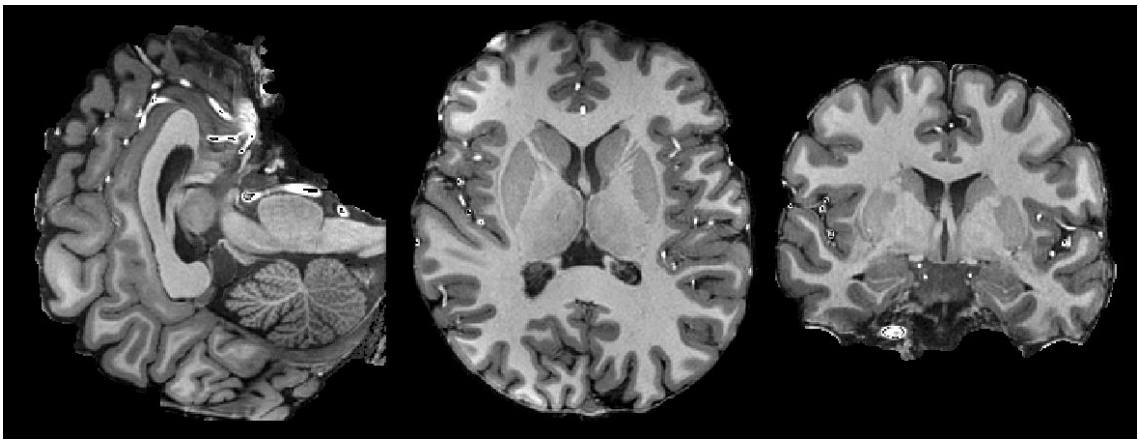

Figure 3.1.1.2 - Slices through a four-scan average structural image. Noise reduction in comparison with Figure 3.1.1.1 is evident in the smoother texture of the homogeneous regions and the more cleanly delineated boundaries.

3.1.2 Bias Field

Although a well-designed MRI scanner will have a homogeneous magnetic field while the bore is empty, the introduction of a person into the scanning field corrupts homogeneity. Inhomogeneous magnetic susceptibility in the person being scanned (e.g., in a human head with several borders between solid, liquid, and gas spaces) changes the strength of the field in and around the person. Additionally, sensitivity variations in the receive coil, especially multichannel coils can affect the homogeneity of the resulting image [4]. While clinical scanner software does an excellent job correcting for this with B1 shimming [5], the higher field strength in our study, and use of multichannel coils, both exacerbate this problem. This means the resulting images are often affected by a low frequency signal variation spanning the FOV of the image. While the human eye is relatively insensitive to this kind of signal variation, many methods of image segmentation (especially those involving a thresholding technique) are heavily corrupted. The below figures show a structural MRI before and after bias field removal using a surface fitting approach [6] as implemented in BrainVoyager. Also shown is the first removed bias field (BrainVoyager fits and removes two bias fields by default).

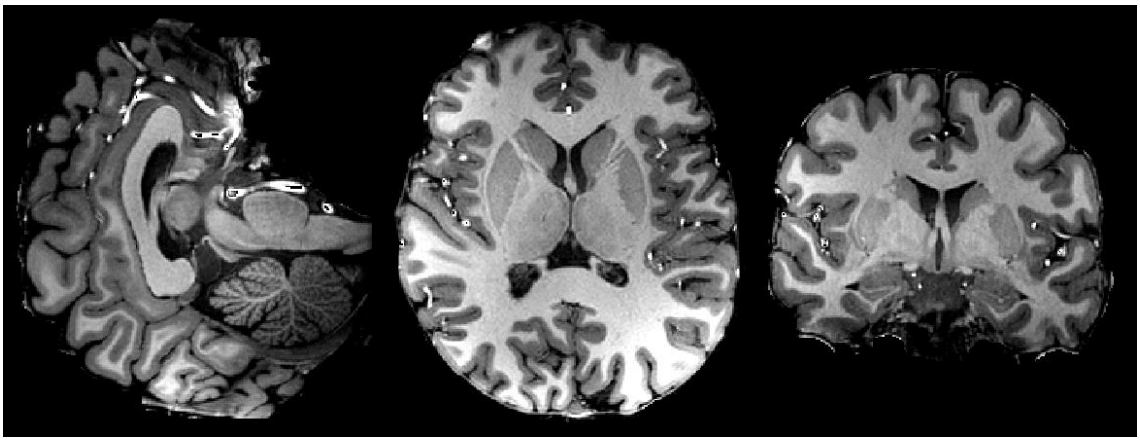

Figure 3.1.2.1 - Slices through the raw structural image following only brain extraction and optimal windowing and leveling. The effect of the bias field is evident in the brighter intensities in the anterior and left lateral regions compared to the frontal and right lateral regions.

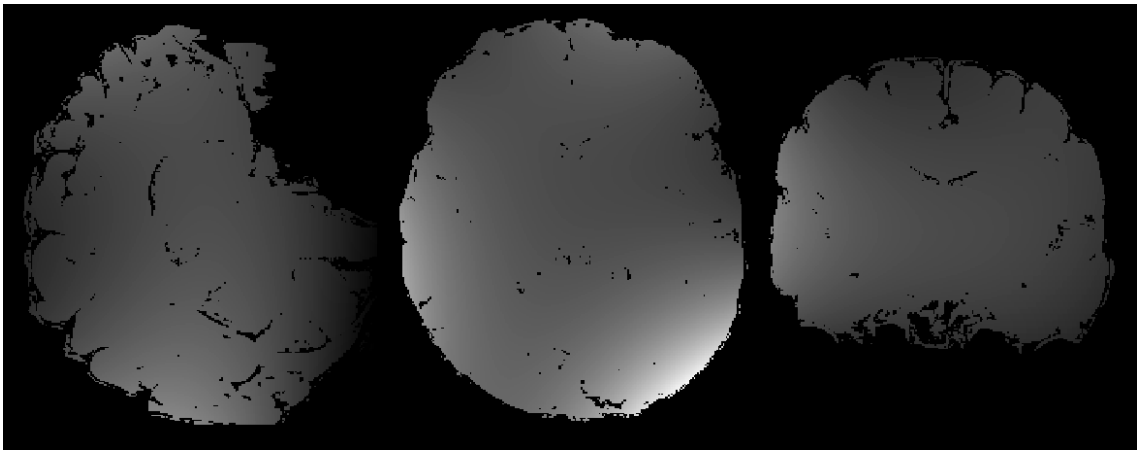

Figure 3.1.2.2 - Slices through the first removed bias field. The regions of high intensity previously noted can be seen in the bias field. One additional rounds of bias field removal was done, but the first bias field corresponds most obviously with the raw image.

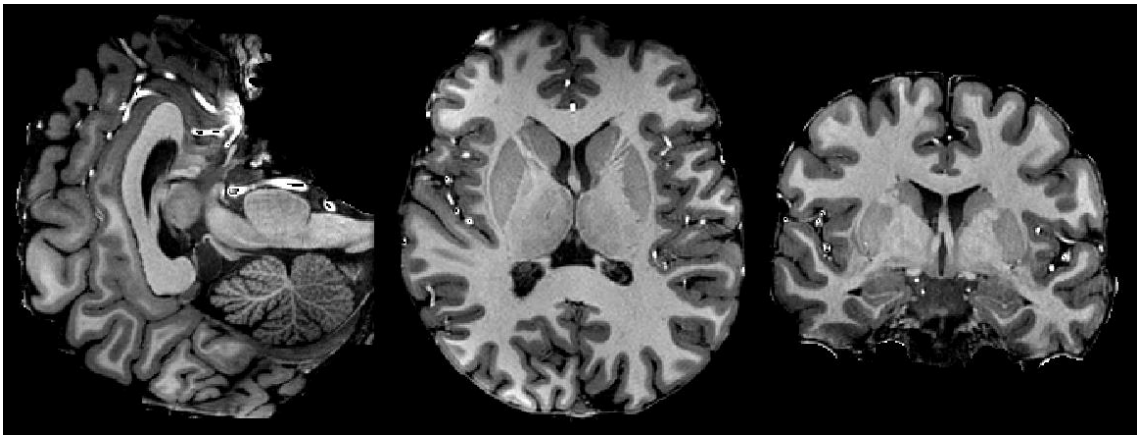

Figure 3.1.2.3 - Slices through the structural image post bias field removal. Compared to Figure 3.1.2.1 it can be seen that the intensity values for grey matter regions and white matter regions are more consistent across the brain.

3.1.3 Partial Volume Effect

The partial volume effect is a phenomenon that occurs when sampling voxels near a boundary between different tissue types. Some voxels will span the boundary, and will sample both tissue types resulting in a signal value in between the two. This results in a loss of contrast between the tissues and the blurring of the boundary.

Primarily, the partial volume effect is combatted with higher resolutions (smaller voxel sizes). As voxel sizes decrease, the number of voxels overlapping a boundary will decrease. Also, very few physiological tissue boundaries are perfectly, sharply delineated, instead having thin regions of transition (true of the grey matter, white matter boundary of the human brain). This means that as voxel sizes approach the size of the physiological boundary region, the closer the boundary shown by the MRI will get to matching the histological boundary.

Structural scans acquired for this project were obtained at an isotropic resolution of 0.6 mm (compared to a commonly used 1 mm isotropic resolution). The below figure from Lüsebrink et al. 2012 [7] (reused with permission from Elsevier, see 3.6 References) shows two images, one acquired at 0.5 mm isotropic resolution and one acquired at 1 mm isotropic resolution. White matter - grey matter boundaries generated from each differ locally. In many of the regions where they differ, each contour looks reasonable against its respective raw image. This is due to the partial volume effect at larger voxel sizes blending the boundary, particularly in regions where the boundary shifts directions multiple times in a small distance (finer anatomical structures).

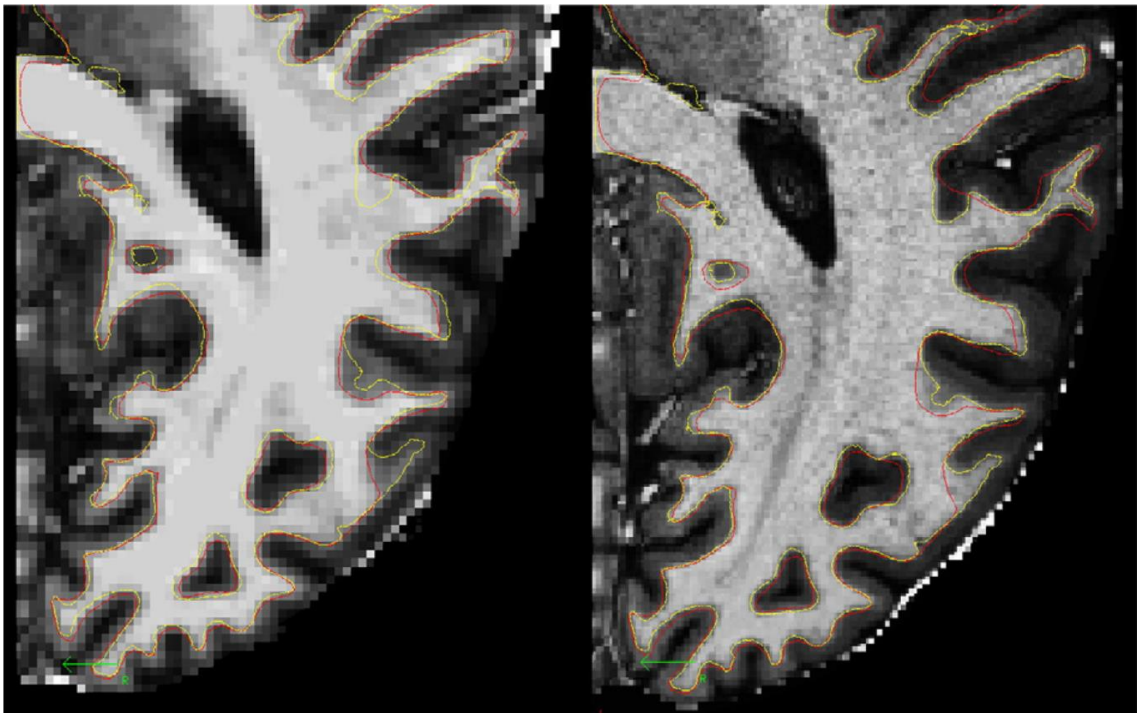

Figure 3.1.3.1 - Axial slices from two scans, of a single subject, both acquired at 7T. The left image has an isotropic resolution of 1 mm and the right image of 0.5mm.The red and yellow contours represent, respectively, the white matter–grey matter boundary derived from the isotropic 1 mm data and the isotropic 0.5 mm data. [7]

3.1.4 EPI Distortion Artifacts

The three previously discussed complications impact the segmentation of the structural images. However, in our project segmented tissue is an intermediate goal. We must also apply this segmentation data to sample information from our functional images. The critical factor to consider here is that registration between the structural and functional images must be good for the segmentation data to sample from the correct location in the functional images. Unfortunately the Echo Planar Imaging (EPI) sequence most commonly used to collect functional MRI data has spatial distortion, as discussed in section 2.4.1.

There are prospective and retrospective methods of minimizing this distortion. Echo spacing can be minimized, but this is in balance with the desired resolution and the BOLD sensitivity of the sequence. In this project we relied on B1 shimming to create as homogeneous a field as possible across the brain. This was done manually and uniquely for each session. Also, the choice to image only one hemisphere of the brain for the functional imaging meant that manual shimming could do an even more accurate job within our FOV. We evaluated the use of field map based undistortion for retrospective correction of the EPIs but found it unnecessary. While some small degree of distortion does exist, particularly around the frontal sinuses, the figures below show that this distortion is not an issue in the region of interest where our resampling occurs.

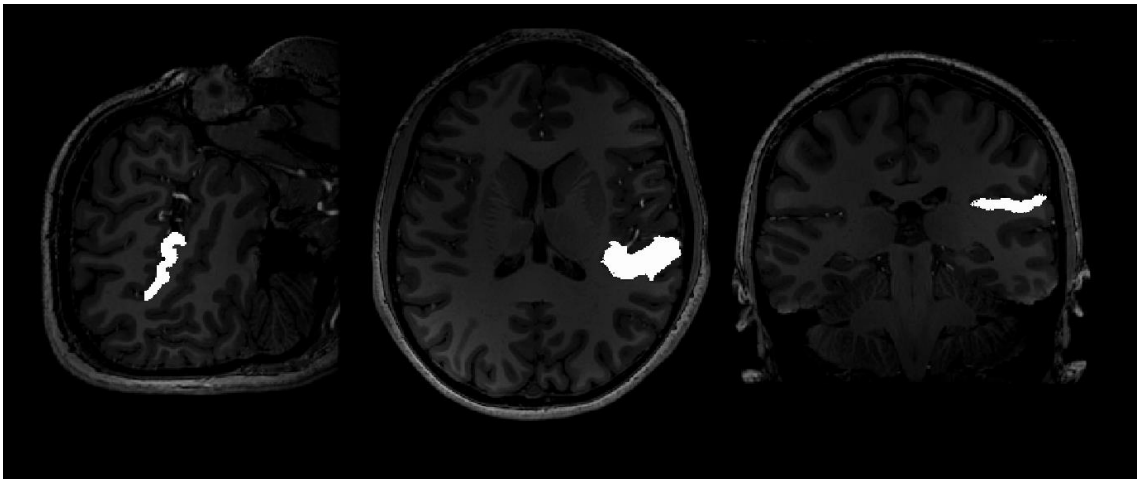

Figure 3.1.4.1 - Slices through a structural image with the vertices of ten structurally derived segmentation grids plotted in white. As the vertices were derived from this image, they are where intended spatially.

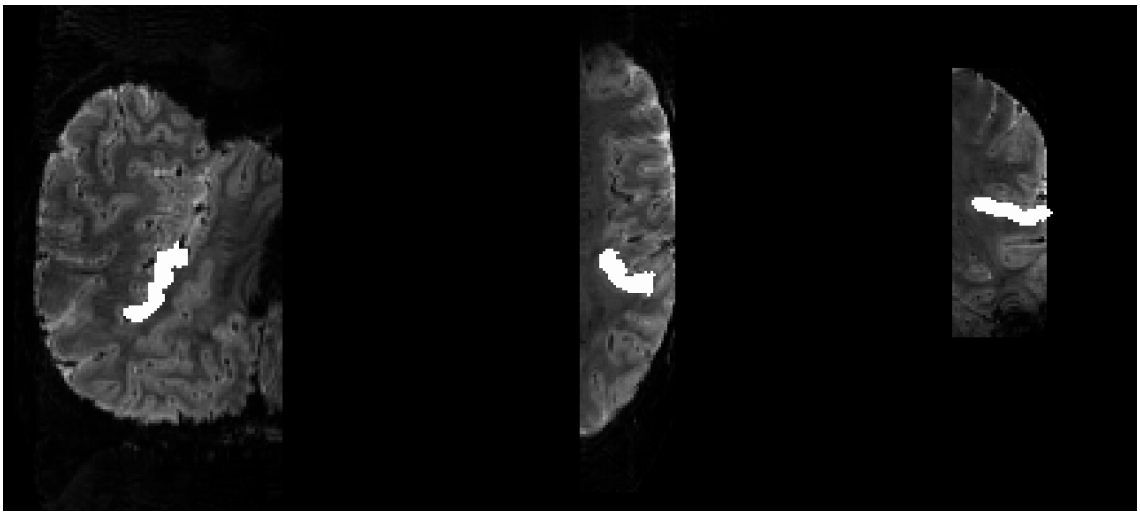

Figure 3.1.4.1 - Slices through a mean functional image showing vertices of ten structurally derived segmentation grids plotted in white. Although being derived from a structural image and transformed to functional space, the vertices still have excellent coverage of the intended regions of grey matter. While some EPI distortion can be seen (frontal region of the axial slice), it has not affected the EPI in the region where the segmentation grids are generated.

3.2 Software Options

Current papers exploring laminar fMRI in humans have utilized different techniques for obtaining laminar specific functional results. All methods must eventually bin or label all grey matter voxels of interest by layer, depth, or some distance measure. One attempted this by manually segmenting only the WM-GM boundary and binning grey matter voxels by minimum Euclidian distance from this boundary [8]. Another manually defined both WM-GM and GM-CSF boundaries repeatedly in 2D and automatically generated fixed distance spaced profiles between the two profiles [9]. Others used automated tools for defining both WM_GM and GM-CSF surfaces and automatically generating thickness maps of a section of cortex. Methods of calculating thickness maps have been explored [10] and while a new "equi-volume" model has been used recently (and most interestingly can be applied directly to EPI images) [11], many papers utilize the "Laplace equation" for determining distance [12,13,14] as implemented in BrainVoyager.

3.2.1 Available Software

Few MRI image analysis software packages include the tools necessary to achieve this project's goal; sampling functional data with structurally derived cortical laminar maps. Several popular packages (SPM, Freesurfer, FSL, and BrainVoyager included) are capable of doing basic cortical segmentation (mapping white matter, grey matter, and CSF), but few take the last steps of generating cortical thickness maps, and generating depth maps based on this data. Other specific problems prevented the use of specific software packages. For example, FreeSurfer has an excellent reputation for segmentation, but it has an outdated problem in that it scales all images to 1 mm isotropic resolutions, even if they're already of a higher resolution. For this reason, BrainVoyager was selected for this project. BrainVoyager has a pipeline of processing tools which include automated cortical segmentation, automated cortical thickness measurements, and automated generation of any number of vertex maps at specified relative depths. This appears to currently be the most comprehensive single tool for this type of analysis.

3.2.2 Contrasts

BrainVoyager's pipeline is designed to work with high resolution T1-weighted structural images. It is interesting to note however, that while EPI images often have weak white/grey contrast in comparison, the high resolution EPIs collected for this project produced mean EPI volumes with very prominent boundaries. Although not investigated in this thesis, future adaptation of BrainVoyager's tools, or new tools could allow segmentation of EPI images directly [11].

3.2.3 Outputs

From the outset of the project it was established that functional analysis would be completed with SPM and the automatic analysis (aa) pipeline [15]. Therefore, the segmentation portion of the analysis needed to result in data which could be integrated into the existing pipeline. While BrainVoyager outputs its depth maps in a proprietary format by default, it can be made to output the data in text format instead, which is well formatted, and easily read into matlab with minimal code.

It should be noted that while BrainVoyager does contain all the tools necessary for completing the functional analysis as well as the segmentation, however it is not easily automated. As the development of the pipeline for this project was a highly iterative process, the fully automated nature of *aa* was highly desirable.

3.3 BrainVoyager Pipeline

This section will briefly describe each of the steps performed with BrainVoyager to obtain our cortical laminae grids. Further details can be found in the BrainVoyager QX User's Guide.

3.3.1 Raw Data Conversion

Raw Data collected from scanning sessions is in NifTI (.nii) format. BrainVoyager utilizes proprietary file formats for each common type of MRI image. Our structural NifTI images are converted to BrainVoyager's 3D Anatomical (.vmr) files with BrainVoyager's NifTI Conversion Plug-In.

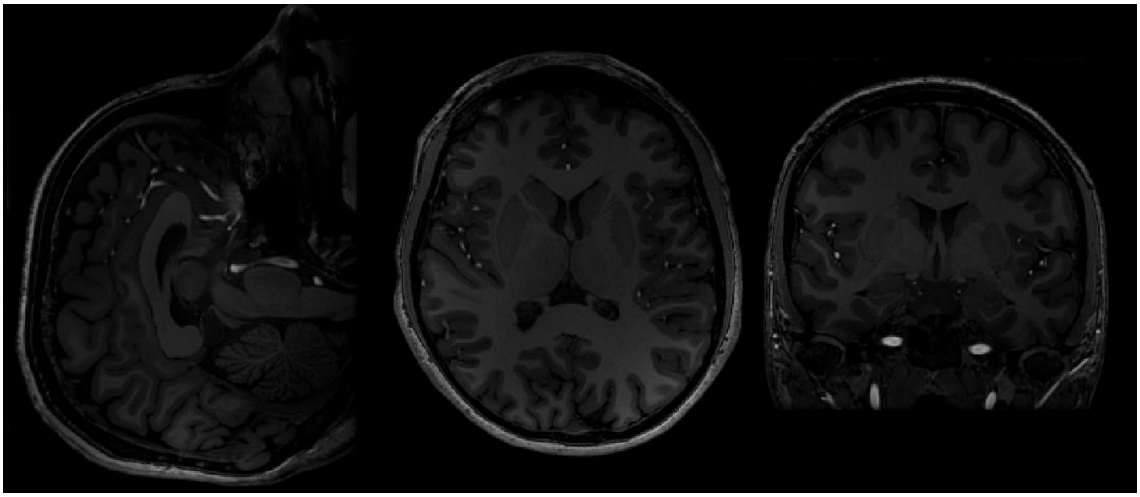

Figure 3.3.1.1 - Slices through a raw structural image after conversion to a .vmr file. No windowing/leveling has been applied.

3.3.2 Intensity Inhomogeneity Correction and Brain Extraction

BrainVoyager begins by "cleaning" the image background, setting all low signal voxels values outside the head to zero. Brain extraction is completed using a combination of binary representations of the image and component analysis, removing the skull and tissues surrounding the brain. Low frequency 3D variations across the brain are then detected and subtracted from the image to correct for local field inhomogeneities as discussed in 3.1.2. This is especially important at high field and with a phased coil array. BrainVoyager then performs a histogram shift to match grey matter and white matter peak values to default values of 100 and 160 respectively. This step is fully automatic and requires no user input.

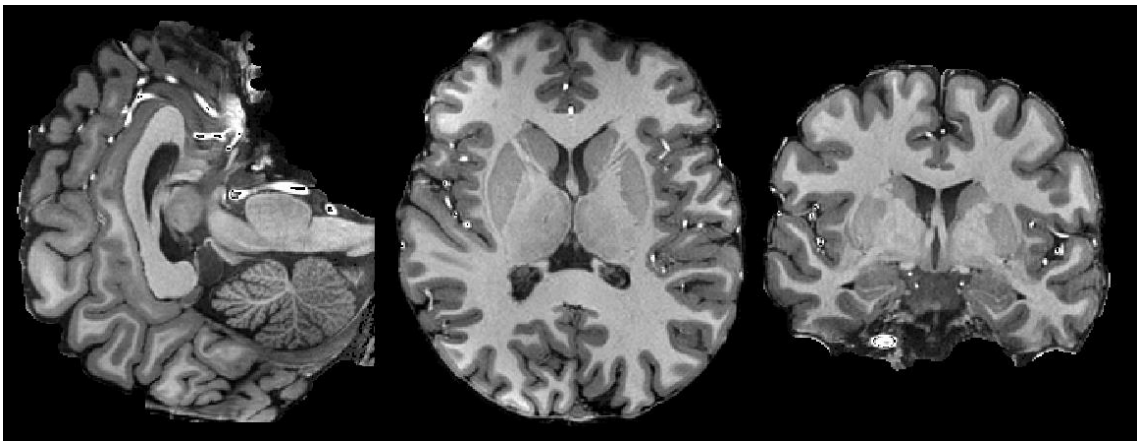

Figure 3.3.2.1 - Slices through a structural image after brain extraction and intensity inhomogeneity correction. Histogram has been shifted to conform with default BrainVoyager values, and the image is thus implicitly windowed and leveled.

3.3.3 Maximum Gradient Maps

Maximum Gradient Maps are calculated. These maps are a first approximation of the boundaries throughout the brain based on non-directional maximum gradient boundaries. This step is fully automatic and requires no user input.

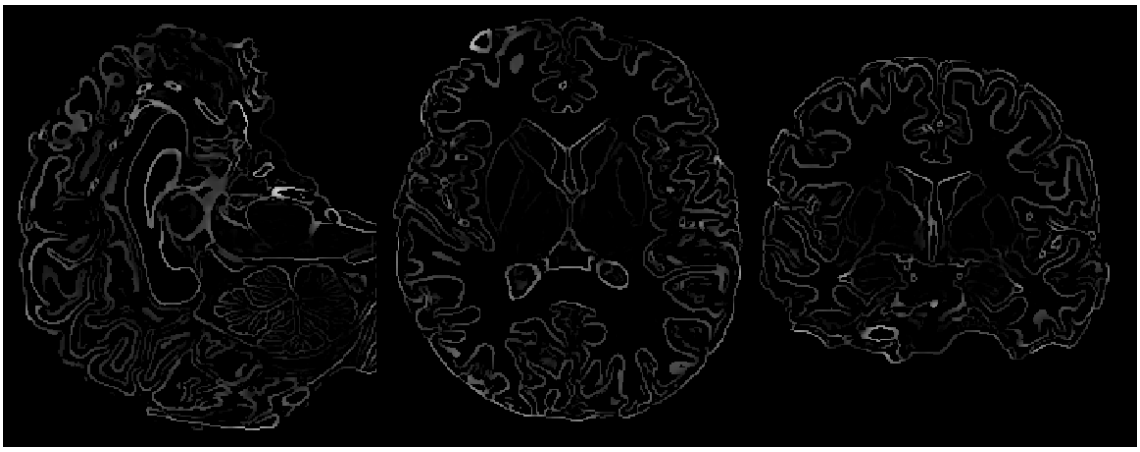

Figure 3.3.3.1 - Slices through a gradient image generated, from a structural image, as an input for the subsequent white matter identification step.

3.3.4 White Matter: Adaptive Region Growing

An adaptive region growing process is then used to identify the white matter in the brain. This process begins by analysing a global histogram of the entire brain to identify peak signal values for grey matter and white matter. It then uses a user inputted Global White Matter Threshold value to pick a threshold value between the two peaks. Voxels above this threshold are then labeled as white matter.

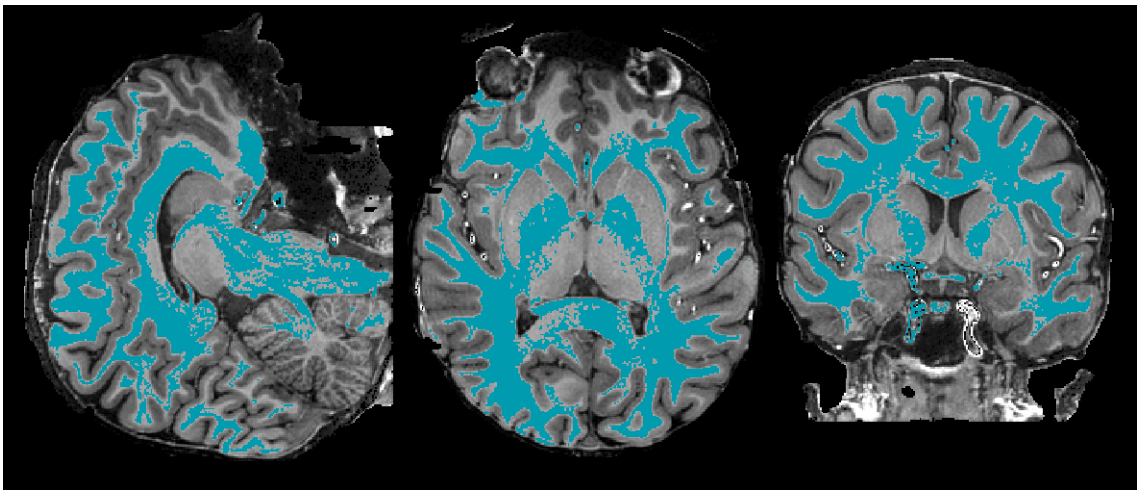

Figure 3.3.4.1 - Slices through a structural image. The blue region indicates voxels identified by BrainVoyager to be white matter by use of the global white matter threshold value.

BrainVoyager then traces the outline of the identified white matter regions and calculates smaller local histograms. It then uses a user inputted Local White Matter Threshold value to pick a threshold value between the two peaks. Within this local region, additional voxels above the new local threshold are added to the white matter mask.

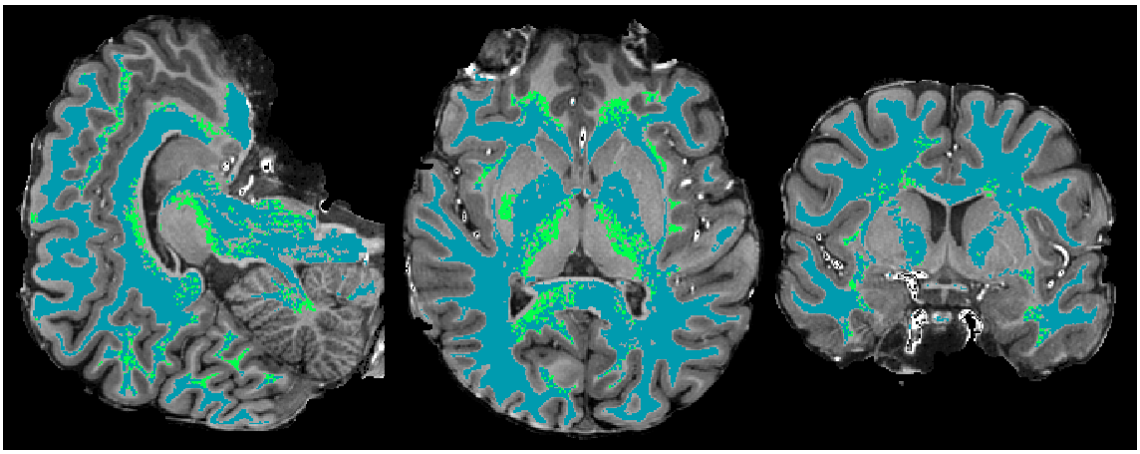

Figure 3.3.4.2 - Slices through a structural image. The blue regions are the same as the previous figure. The green regions are those voxels identified to be white matter by application of a local white matter threshold value.

A polishing step merges the voxels identified by the global and local threshold steps and, using a magnitude map based on computed gradients, smooths the edges of the resulting white matter mask.

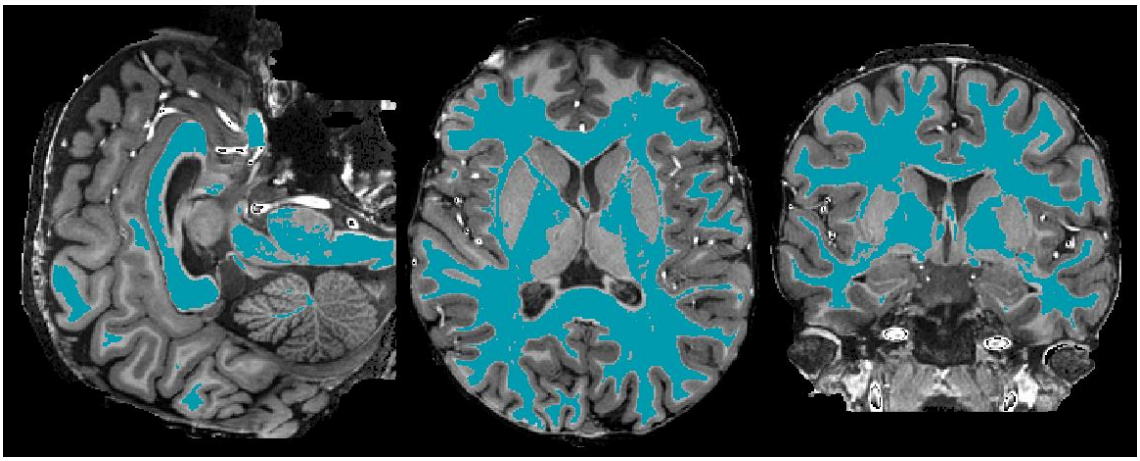

Figure 3.3.4.3 - Slices through a structural image. The blue region is a combination of the blue and green regions from the previous figure, with edge smoothing applied. Note that although many white matter voxels have not been labelled, the threshold values we are using have been specifically identified to optimize labelling in the auditory areas (explained in section 3.4).

3.3.5 Grey Matter: Dilation

To identify the outer grey matter border, BrainVoyager performs a dilation from the previously identified WM-GM border. User inputted parameters at this step include "Number of Dilation Steps", "Stop Crit Left From GM Peak", and "Local Stop Criterion". These parameters lack explanation in the BrainVoyager documentation, but the following assumptions seem reasonable. The "Number of Dilation Steps" dictates how many steps (voxelwise) are taken outwards from the WM-GM border. This should only be important when the background signal values are close to the grey matter values, or extremely noisy. The "Stop Crit Left From GM Peak" will dictate a global histogram defined threshold used to separate Grey Matter voxels from CSF voxels. The "Local Stop Criterion" will dictate a regional histogram derived threshold to allow additional voxels to be included in the grey matter mask.

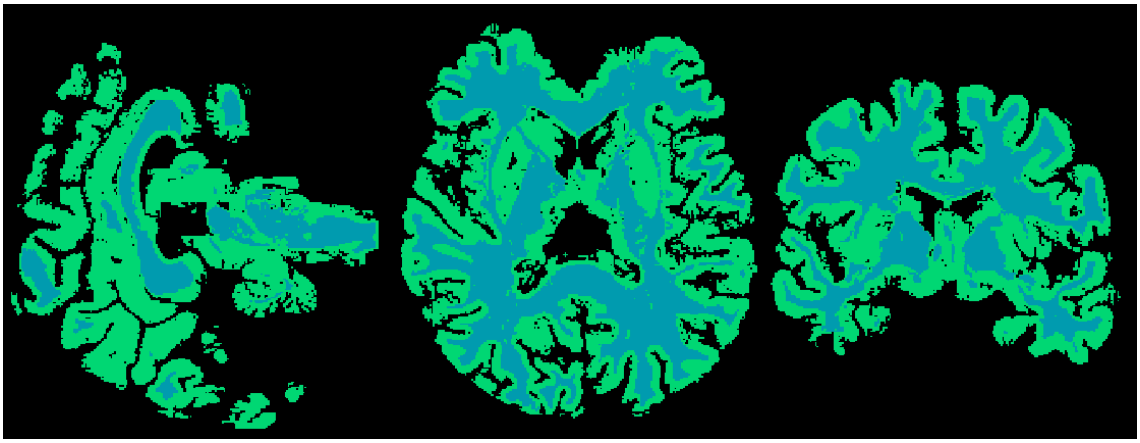

Figure 3.3.5.1 - Slices through a structural image. Blue regions indicate the final selection of white matter voxels from the previous steps. Green regions indicate those voxels identified to be grey matter voxels by the dilation process.

A polishing step similar to that used in the white matter identification uses magnitude maps based on gradient maps to smooths the edges of the grey matter mask.

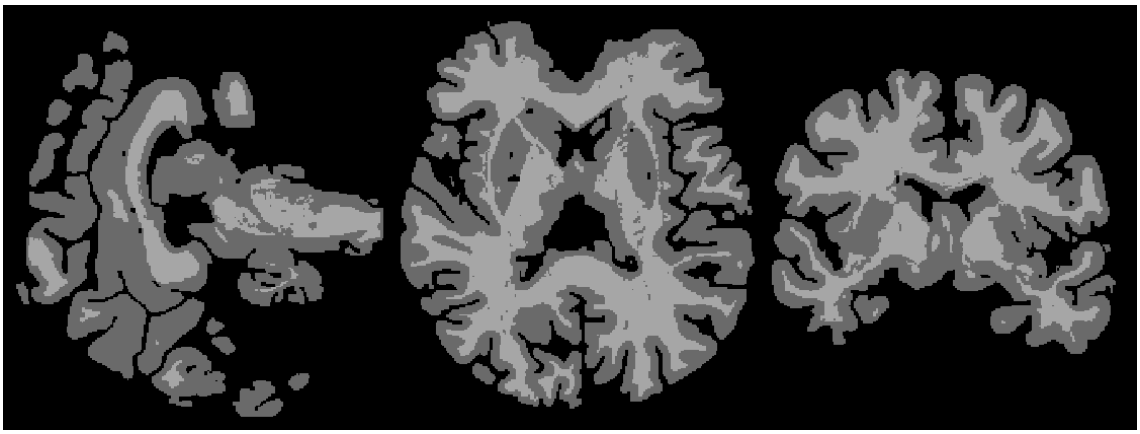

Figure 3.3.5.2 - Slices through a structural image. Light grey regions indicate the final selection of white matter voxels from the previous steps. Dark grey regions indicate the grey matter voxels identified in the previous figure after edge smoothing.

3.3.6 Cortical Thickness Measurement

Cortical Thickness throughout the grey matter is then calculated automatically. BrainVoyager performs these calculations using the Laplace Method as described in [16].

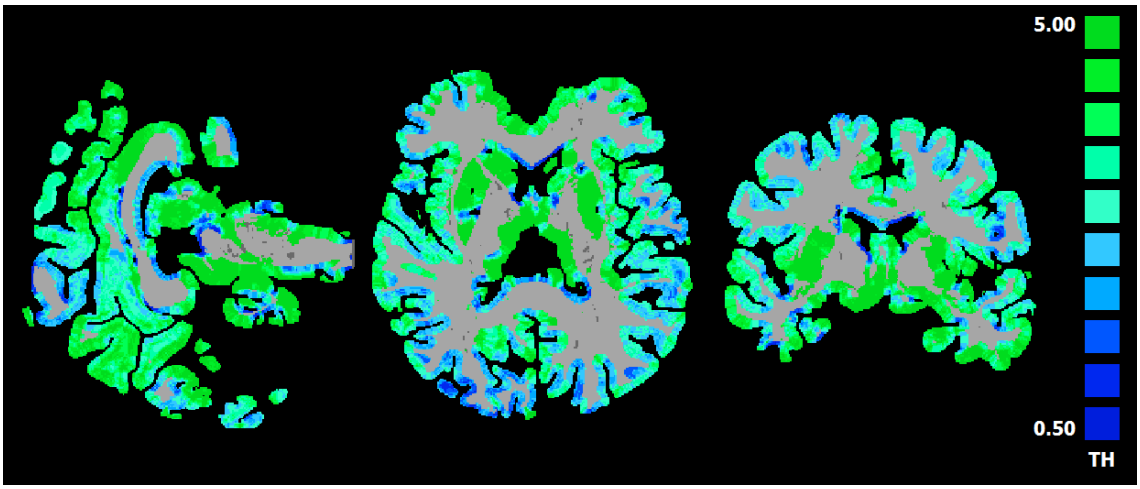

Figure 3.3.6.1 - Slices through a structural image. Grey regions indicate white matter voxels. The colored regions indicate grey matter voxels where the local cortical thickness is specified by the color as referenced from the color bar on the right in voxels.

3.3.7 High Resolution Cortex Grid Sampling

BrainVoyager's "High Resolution Cortex Grid Sampling" tool is then used to create regularly sampled grids at specified depths in the grey matter. The grid sampling tool first creates a regular spaced grid at the middle layer of the cortex and then creates subsequent grids by moving up or down grid points along streamlines to get corresponding grid points for other relative depth levels. This means the grids at all layers cover the same regions of cortex, and have one-to-one correspondence between points. It does however mean that the exact distance between points for all grids other than the middle layer will be slightly larger or smaller depending on local cortex curvature. While it is possible to instead constrain point spacing, having corresponding grids across layers is more important for later functional analysis and visualization. Any number of grids up to 10, with any degree of spacing between them, is user inputted. These grids can be generated within a VOI or centered on a particular point. Our pipeline generated 10 grids evenly spaced between 0 (the WM-GM border) and 1 (the GM-CSF border) centered on a predetermined voxel. The resulting grids can be viewed in 2D on any previously created image, or in 3D using openGL tools with cross sections of any previously generated image.

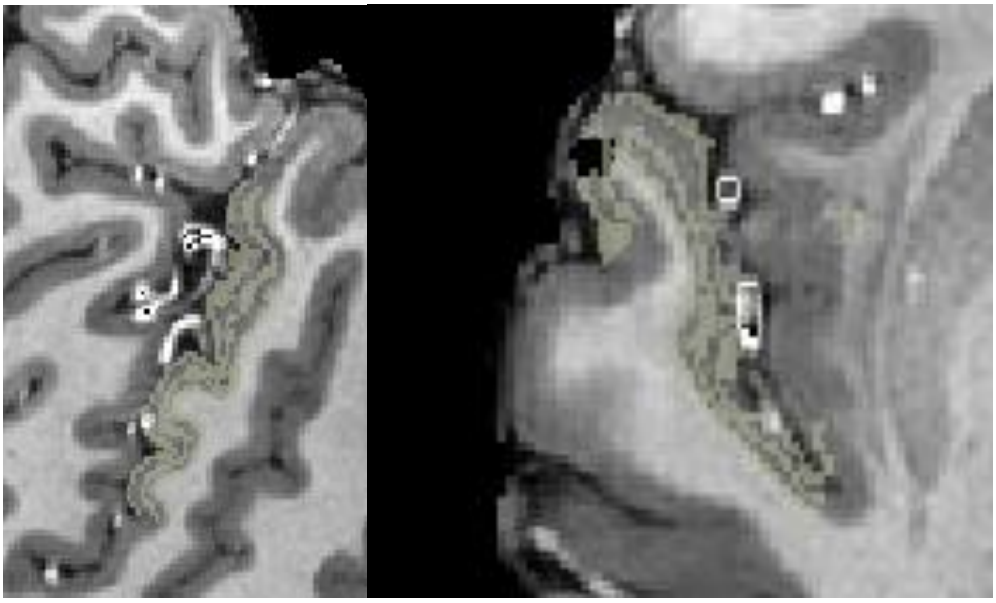

Figure 3.3.7.1 - Sagittal and axial slices through a structural image. In the auditory region on each slice are three beige grids that correspond to surfaces 0%, 50%, and 100% of the distance between the WM-GM boundary and the GM-CSF boundary.

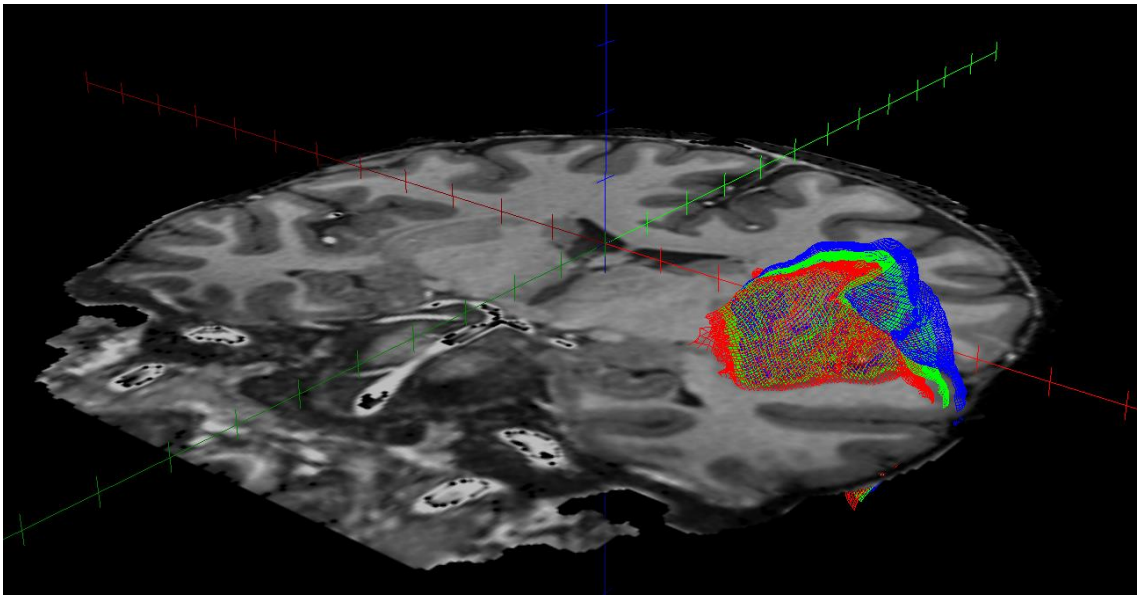

Figure 3.3.7.2 - The same three grids as in the previous figure rendered in 3D with a 2D coronal slice for reference.

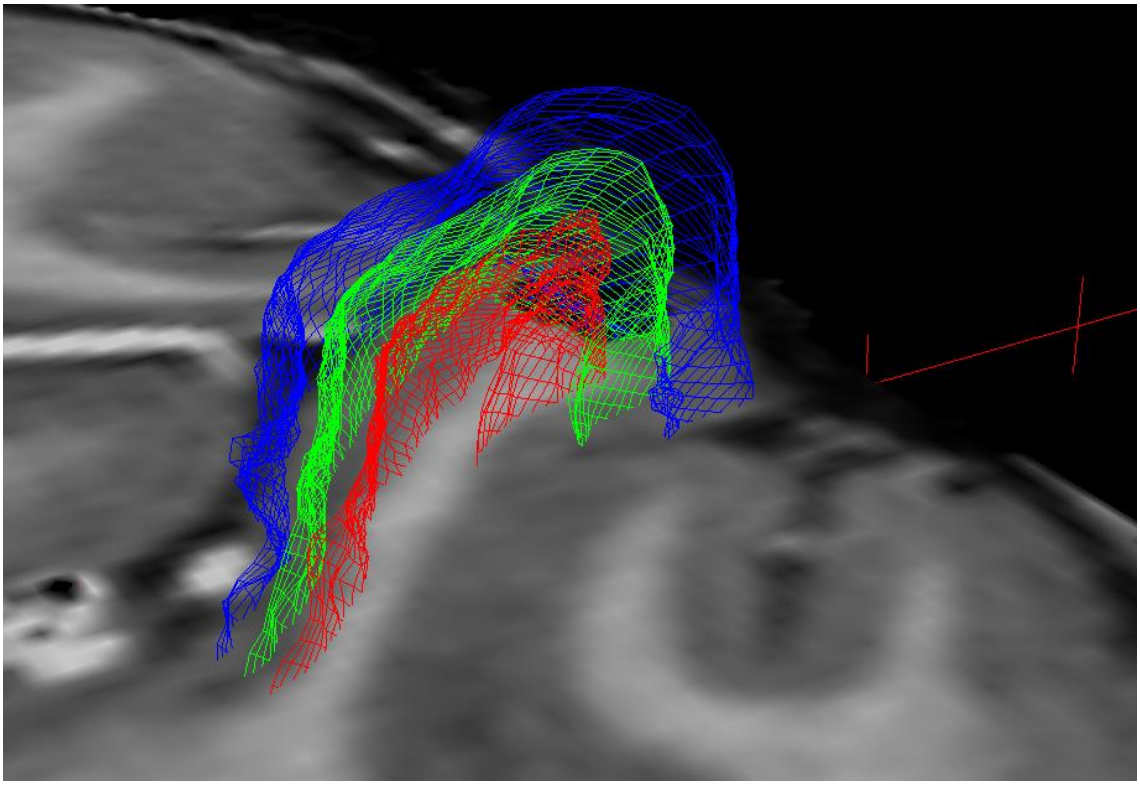

Figure 3.3.7.3 - A close-up of the three grids mentioned in previous figures visually demonstrates their alignment with particular depths of grey matter.

3.4 Pipeline Optimization

As mentioned previously, the BrainVoyager pipeline for generating cortical laminae grids has several steps which require user input. Specifically, values for global white matter threshold, local white matter threshold, global grey matter threshold, and local grey matter threshold can have large impacts on the resulting cortical laminae grids. While BrainVoyager provides default values for these inputs, we wished to investigate whether modifying them improved accuracy. To do this we developed optimization tools and methods to quantitatively determine the best choices for these inputs.

3.4.1 Custom MtA Matlab Tool

To quantify the accuracy of the BV grids, a Manual to Automatic (MtA) comparison tool was created. This MATLAB tool allows the manual selection of any number of points along the White Matter - Grey Matter (WM-GM) boundary and the pial

surface (Grey Matter - Cerebral Spinal Fluid (GM-CSF)) in a number of slices overlapping the region covered by the BV grid. The tool then determines the nearest neighboring vertex from the BV grid to each of the manually inputted points. The distances between these points are calculated, both as a single Euclidean distance, as well as a set of Cartesian unit vectors.

The measures the MtA tool extracts are described as follows.

Absolute distance between manually selected WM-GM points and corresponding nearest neighbor points on the BV WM-GM grid are found. The median of these distances quantifies the error in the grid, and the standard deviation of these distances quantifies how variable grid errors are. The same values are shown for the GM-CSF grid. The objective for optimization was created by taking the root mean square (rms) of the resulting median and standard deviation of the distance measure, $\sqrt{\frac{1}{2}(med^2 + std^2)}$,as both are values we want to minimize in parameter selection

The *Cartesian bias vector* was found by taking the median x, y, and z displacements between the manual points and the BrainVoyager grid. Because the x, y, and z vectors could be positive or negative, the spread of these values can centre on zero. This allows us to get an idea of whether our BrainVoyager grid is very close to the manually selected points with error on both sides of this surface (in which case the value will be closer to zero than the absolute distance value) or whether our BrainVoyager grid is entirely positioned on one side of our manually selected points (in which case the value will be similar to the absolute distance value). The median of these three vectors is found to give a sense of the error in the grid in each direction. The standard deviation of these values is also found to get a sense of the variability of this measurement. A summary optimization value is found by first taking the rms of the median and standard deviation is each direction, and then the rms of these three values, $\sqrt{\frac{1}{3}\left(\sqrt{\frac{1}{2}(med_x^2 + std_x^2)}^2 + \sqrt{\frac{1}{2}(med_y^2 + std_y^2)}^2 + \sqrt{\frac{1}{2}(med_z^2 + std_z^2)}^2\right)}$, yielding a

number sensitive to both the error in the grid in each direction and the spread of that data in each direction.

By running the same scan through BrainVoyager using a spectrum of input parameters to create a set of grids, and running all of these grids through the MtA tool, we were able to plot MtA measures against a range of inputs for a particular parameter, and thus find an optimal choice for that parameter. For example, while leaving all other parameters the same, one could choose six different values for global white matter threshold. The same scan is run through BrainVoyager with each of these values yielding six different grids. These grids are run through the MtA tool, with points being manually selected from several evenly spaced planes through the region covered by BrainVoyager cortex grids. The following figure is an example of one of these slices from the MtA tool.

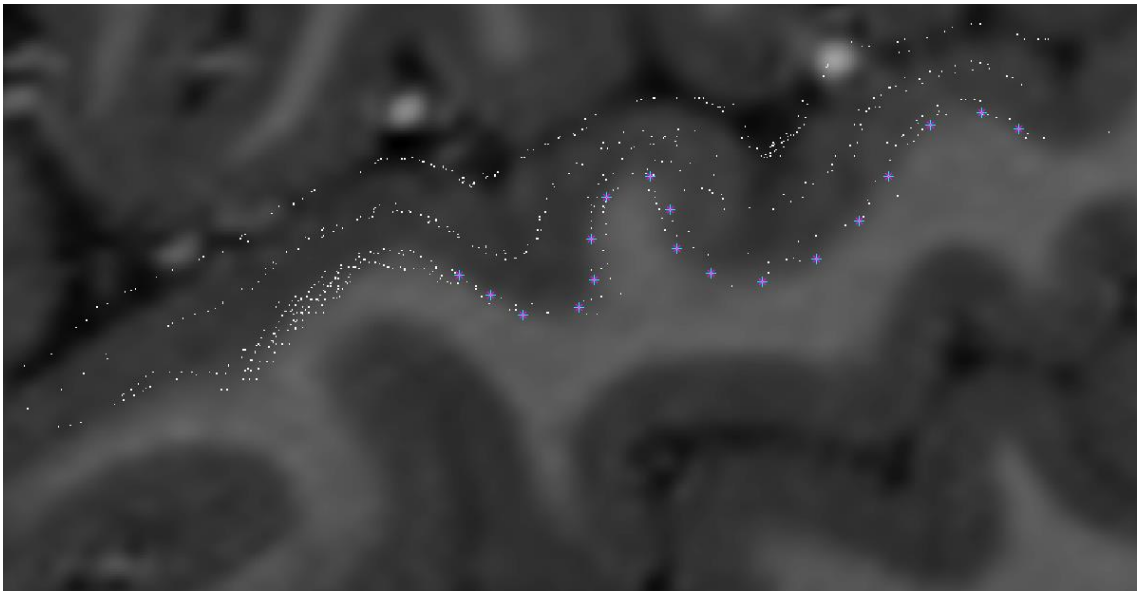

Figure 3.4.1.1 - An example image as would be worked with using the MtA tool. White pixels indicate vertices from the BrainVoyager generated cortical grids, while the blue/red crosses indicate points manually selected by the user to correspond to the WM-GM boundary.

The figure shows a sagittal cross section through the Heschl's Gyrus of one of our scans. The original data have been sinc interpolated by a factor of 10 to produce the

image as shown. The white points correspond to points from all six of the grids produced by BrainVoyager using the spectrum of white matter global threshold values. It is possible to get a sense from this figure of the effect on the WM-GM grids of changing input parameters - note the thicker band of cortex which each grid takes up. You can see that the white matter threshold values also have an effect on the mid-cortex surface, as it's relative to the two outer surfaces. It does not however seem to have a significant effect on the GM-CSF border, as expected given the default grey matter threshold values are being maintained. The colored points on the image are user selected points corresponding to the WM-GM boundary. This is a sample of a selection which would ideally cover the length of the border within the boundaries of the BrainVoyager Grid points. This selection process is repeated for many slices and both the WM-GM and GM-CSF boundary to provide a distribution of manually segmented points across the whole of the BrainVoyager grids.

We first used this tool to assess the accuracy of the BrainVoyager grids created using default input parameters (white matter global threshold 0.6, white matter local threshold 0.5, grey matter local threshold 0.2, grey matter local threshold 0.2, each explained in next section).

Distance (voxels)	Boundary	Median	Standard Deviation	Optimization
Absolute Distance	WM-GM	0.75	0.51	0.64
	GM-CSF	0.79	0.84	0.82
Unit Vector Distance (x/y/z)	WM-GM	-0.35 / -0.15 / 0.17	0.59 / 0.45 / 0.50	0.40
	GM-CSF	-0.40 / -0.17 / -0.16	0.84 / 0.60 / 0.65	0.53

Table 3.4.1.1 - Measures generated by the MtA tool to assess the accuracy of the BrainVoyager generated cortical maps using default parameters.

3.4.2 Number of Averages

With the MtA tool developed, we were first interested in using it to assess the effect of our scan averaging on image noise in the structural volume. To compensate for image noise (discussed in 3.1.1), increased by our use of very small voxel volumes, multiple scans were acquired, realigned, and averaged to produce one structural image to run segmentation on. In theory, image averaging increases SNR by a factor of $\sqrt{N}$ where N is the number of images being averaged. In practice this doesn't hold perfectly true. While the thermal noise in the system is accurately approximated by a Gaussian distribution, and thus random, our images also contain nonrandom physiological noise, and may contain very small shifts in anatomy between individual scans due to subject movement. Thus our resulting increase in SNR will be slightly less than ideal.

Four structural scans were acquired. To assess the benefit of averaging them together, it was decided to examine the impact on segmentation directly, as the precise relationship between image SNR and segmentation is unclear. By averaging together the scans in different numbers and orders, four examples of each of one-scan, two-scan, and three-scan averaged images were created. These twelve scans, along with the single possible four-scan average image were fed through our segmentation pipeline to create surface grids for the white matter - grey matter (WM-GM) boundary and grey matter - cerebral spinal fluid (GM-CSF) boundary. The MtA tool is then used to compare all 13 surfaces.

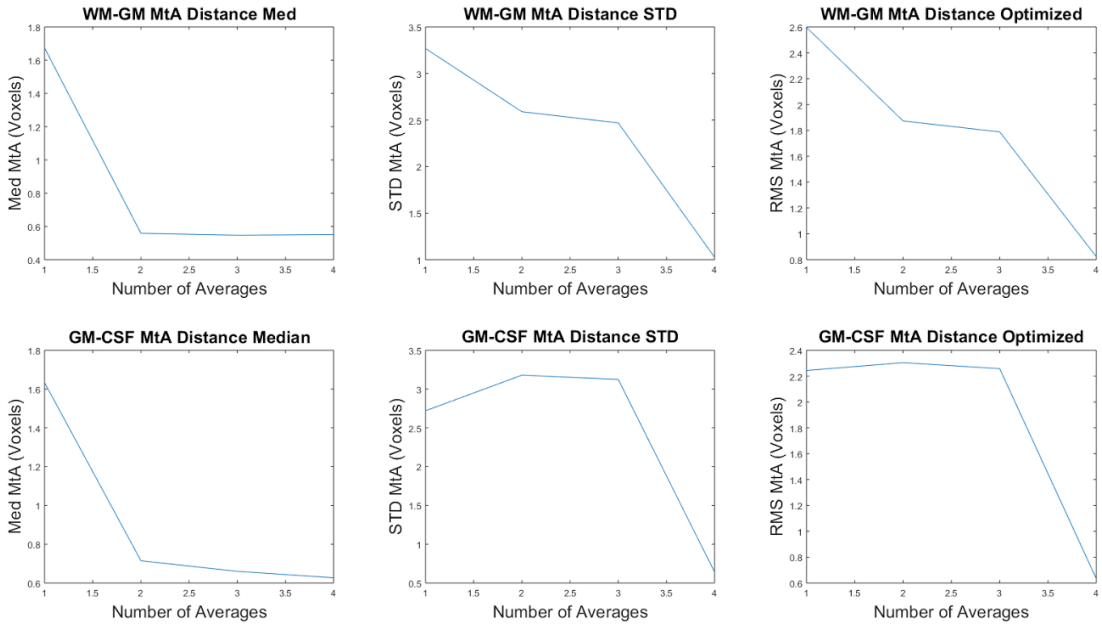

Figure 3.4.2.1 - Results from the MtA tool for differing numbers of averaged scans. The top row is results from the WM-GM boundary, and the bottom row from the GM-CSF boundary. The first column shows the median distance between automatically determined vertices and manually identified vertices. The second column shows the standard deviation of the distances between automatically determined vertices and manually identified vertices. The third column shows an optimization value of the last two (RMS of median value and standard deviation value). All units are in voxels. The points shown for 1, 2, and 3 averaged images are an average from four different images run through segmentation. The point shown for 4 averaged images is from a single image run through segmentation. Manual points selected from a four-scan average image.

The above figure shows a steady improvement (as measured by an optimization value in the third column) in automatic segmentation accuracy for the WM-GM boundary as more scans are averaged together, and a rather sharp improvement at 4 averaged scans for the GM-CSF boundary.

One concern regarding the above measurements was that the manually chosen points were selected from the four-scan average image. This could mean that the automated measures were only improving with more averaged scans because the image

was approaching the image used to define the manually selected points. To make sure that this wasn't the case, the process was repeated using manually selected points selected from a single scan average image.

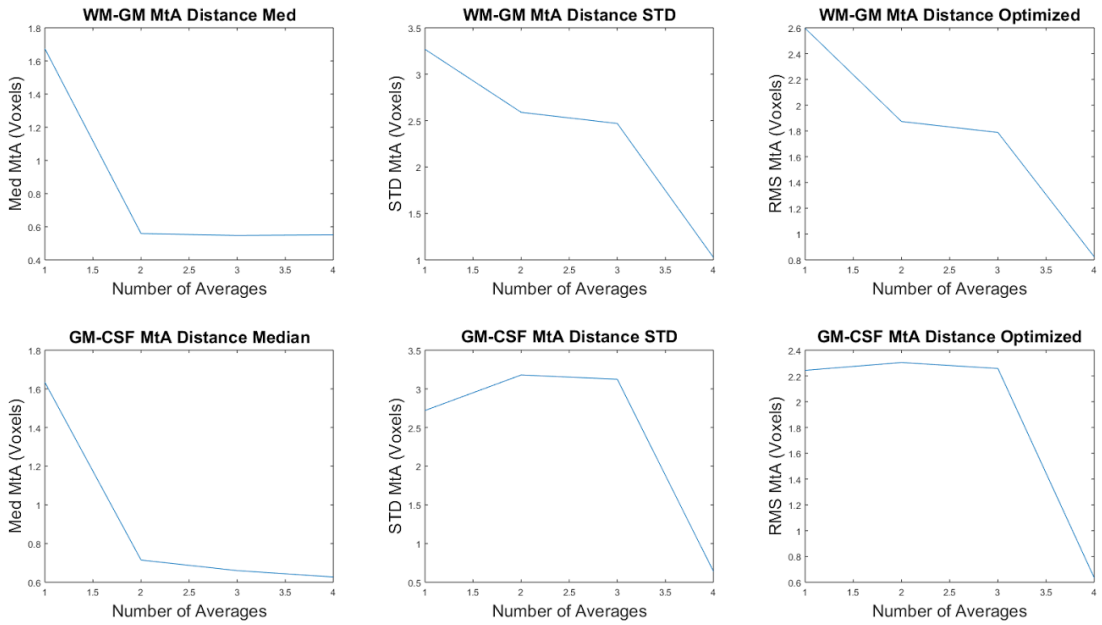

Figure 3.4.2.2 - Results from the MtA tool for differing numbers of averaged scans. The top row is results from the WM-GM boundary, and the bottom row from the GM-CSF boundary. The first column shows the median distance between automatically determined vertices and manually identified vertices. The second column shows the standard deviation of the distances between automatically determined vertices and manually identified vertices. The third column shows an optimization value of the last two (RMS of median value and standard deviation value). All units are in voxels. The points shown for 1, 2, and 3 averaged images are an average from four different images run through segmentation. The point shown for 4 averaged images is from a single image run through segmentation. Manual points selected from a one-scan average image.

Comparing the two above figures, there are no visible differences (although it was confirmed individual data points did differ by very small amounts in the raw data, the differences are not noticeable after averaging). This implies that when manually delineating the two boundaries, the benefit from averaging scans together is negligible,

but the algorithm used for automated segmentation is much more dependent on the image noise reduced through scan averaging.

Some time was spent trying to determine where in the automated segmentation pipeline the effect of averaging was having the largest effect. Two steps stood out. During the histogram shift (see section 3.3.2) noisier images (particularly some of the one-scan images) were sometimes observed to map to peak grey matter and white matter values slightly incorrectly. As subsequent steps seem to assume these peak values, this can shift the location of the tissue boundaries by small amounts. Secondly, during the white matter and grey matter identification steps (see sections 3.3.4 and 3.3.5), more salt & pepper like noise (single voxels of particularly lower or higher signal from the surrounding tissue, more prevalent in the single scan images) was sometimes able to shift the boundaries around one or more particular voxels. More noise impervious histogram shifting methods could be valuable to examine in the future.

3.4.3 Optimizing White Matter Global Threshold Values

We followed this procedure to optimize first the Global White Matter Threshold (WMG) used in the region growing procedure which creates identifies and creates a white matter mask of the brain. This threshold represents a proportional value between the GM peak value and the WM peak value as determined by a histogram of the entire brain. Therefore a threshold value of 0 would match the grey matter peak value, and a threshold value of 1 would match the white matter value. BrainVoyager specifies a default value of 0.6 for this parameter; an intuitively slightly conservative choice nearly halfway between the two peaks.

Values between 0.5 and 1.0 were used to generate 6 BrainVoyager cortex grids. These grids were run through the MtA tool, with points manually selected from 31 evenly spaced planes through the region covered by BrainVoyager cortex grids. The Local White Matter Threshold (WML) was set to 1.5 for this set, which is such a conservative value that the second round of local thresholding will add no additional voxels to the mask and therefore will not obscure the optimization of the WMG Threshold. All other user inputted values were left at the BrainVoyager defaults. To demonstrate the MtA data

for 6 grids, rather than tabulating all the data, we can graph the median MtA distances and their standard deviations for each grid.

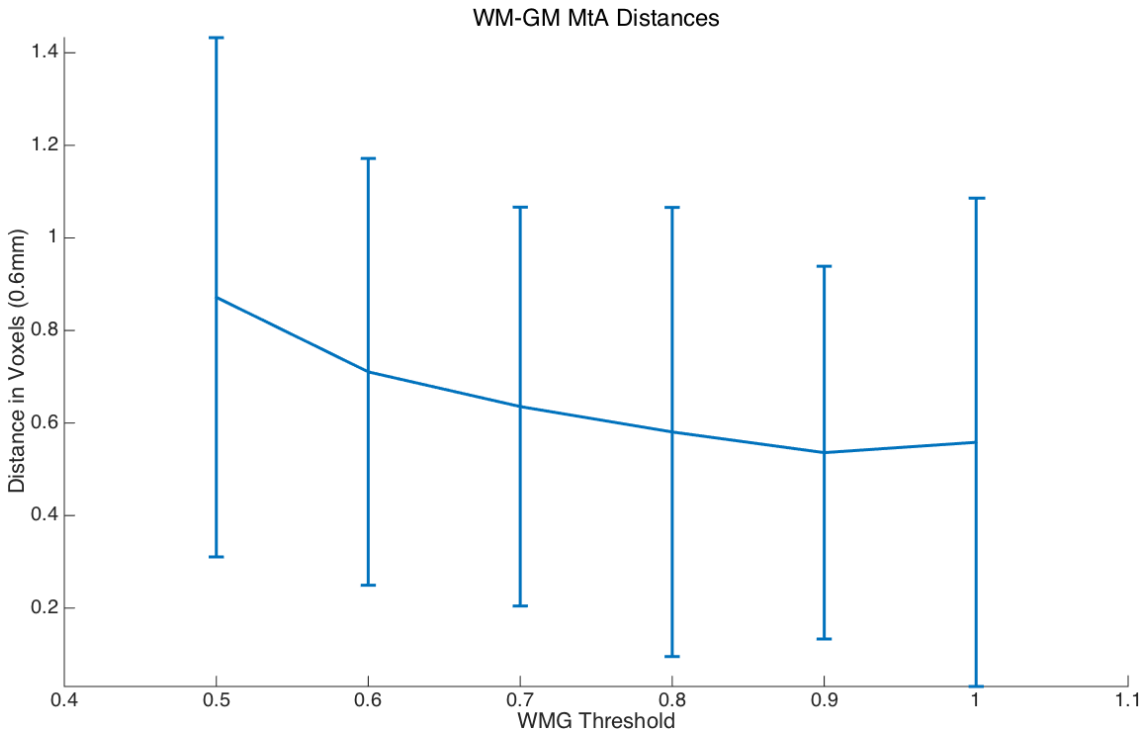

Figure 3.4.3.1 - Median distance in voxels from BrainVoyager generated WM-GM vertices to manually selected vertices using a spectrum of global white matter threshold values. Error bars show standard deviations.

As expected we get an optimization curve in which values at either extreme are less accurate than a moderate value. It can be seen that our lowest MtA distance offers a decrease in MtA distance of 25% compared to the default value. By taking the rms of the median and standard deviation we can obtain an optimization measure for each.

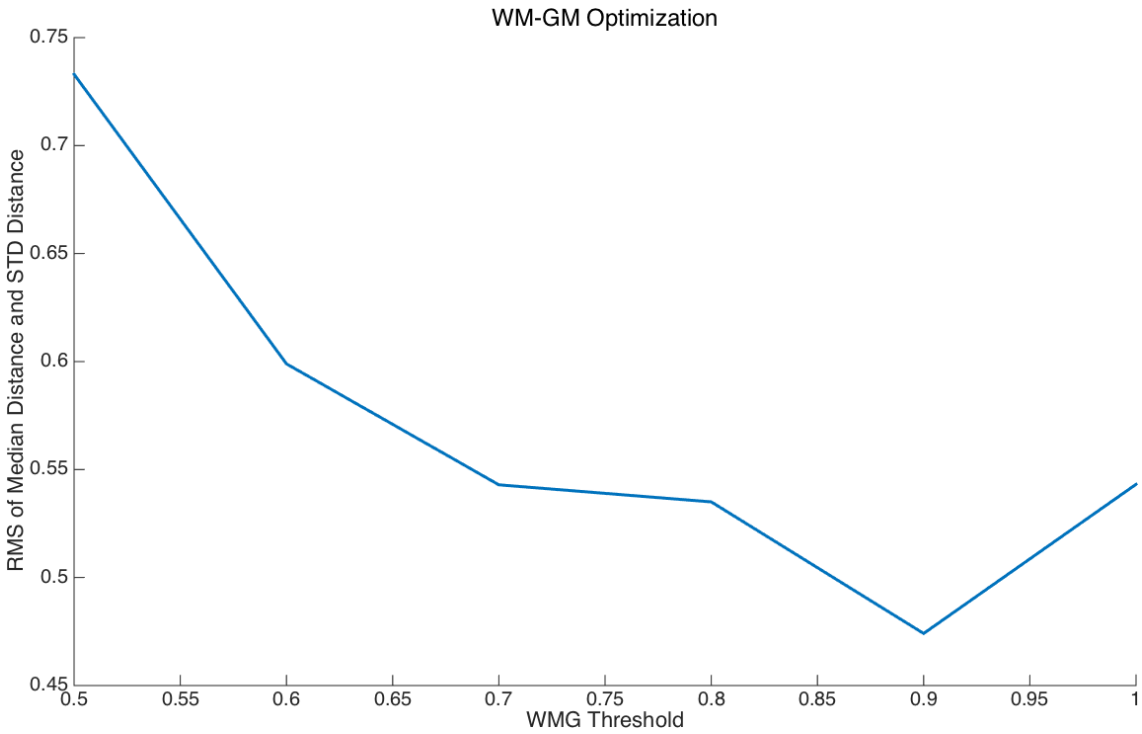

Figure 3.4.3.2 - WM-GM grid optimization measure using a spectrum of global white matter threshold values.

This graph shows, as could likely be predicted from the previous figure, that a GMG of 0.9 provides the most accurate results.

The absolute distance measure shown in Figure 3.4.3.1 does not separate biased (i.e., points clustered systematically on one side of the real boundary) from unbiased noise (i.e., points positioned close to real boundary with error on both sides) of whether each grid is. To capture this we also calculated Cartesian bias vector MtA distance measurements. Plotting these values as histograms allows us to visualize whether the spread of data is centred on zero, as opposed to mostly to the positive or negative side.

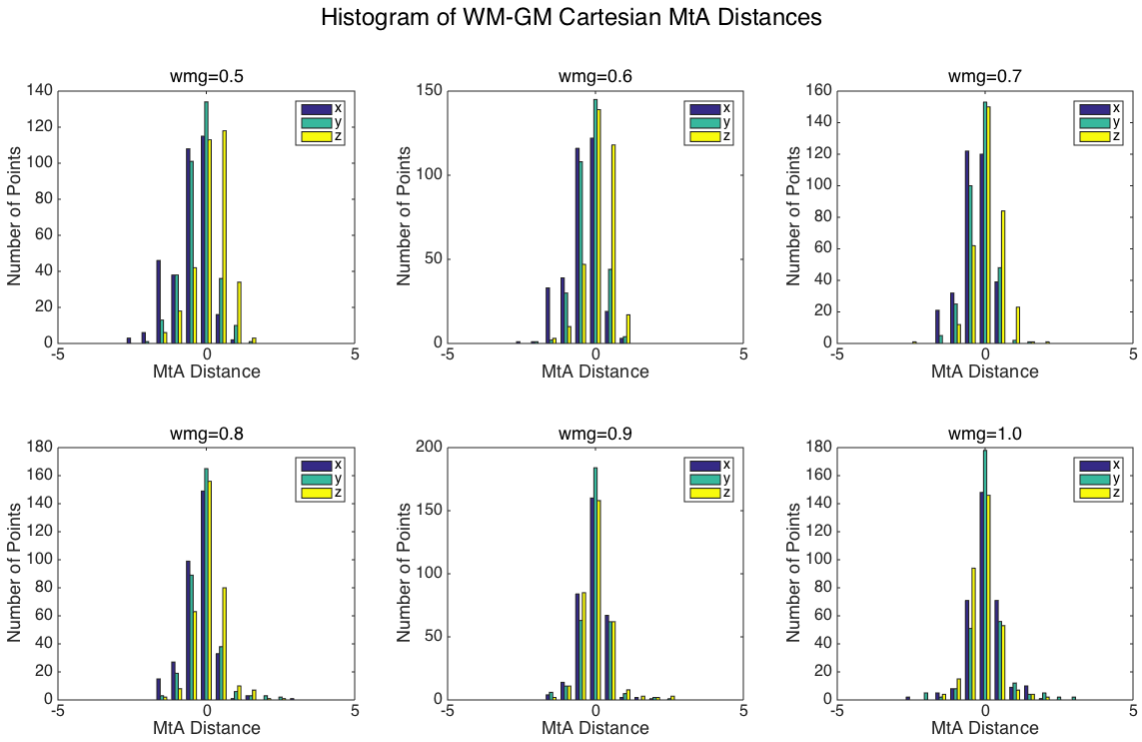

Figure 3.4.3.3 - Histograms of distances in the x, y, and z directions between BrainVoyager generated WM-GM vertices to manually selected vertices using a spectrum of global white matter threshold values.

This series of Histograms shows a few things. For some of the weaker performing values (i.e. wmg=0.5 to wmg=0.7), individual direction histograms are centred on non-zero values, showing the boundary estimation is biased and not just noisy. However, for the better performing threshold values (i.e. wmg=0.8 to wmg=1.0), all three Cartesian directions are centred on zero. This implies that our grids for these thresholds are in fact very close to our manually delineated border, and the median error is due mostly to unbiased noise.

To summarize these histograms without losing the subtlety of separating the directions, we can break the data down into medians and standard deviation for each direction for each grid.

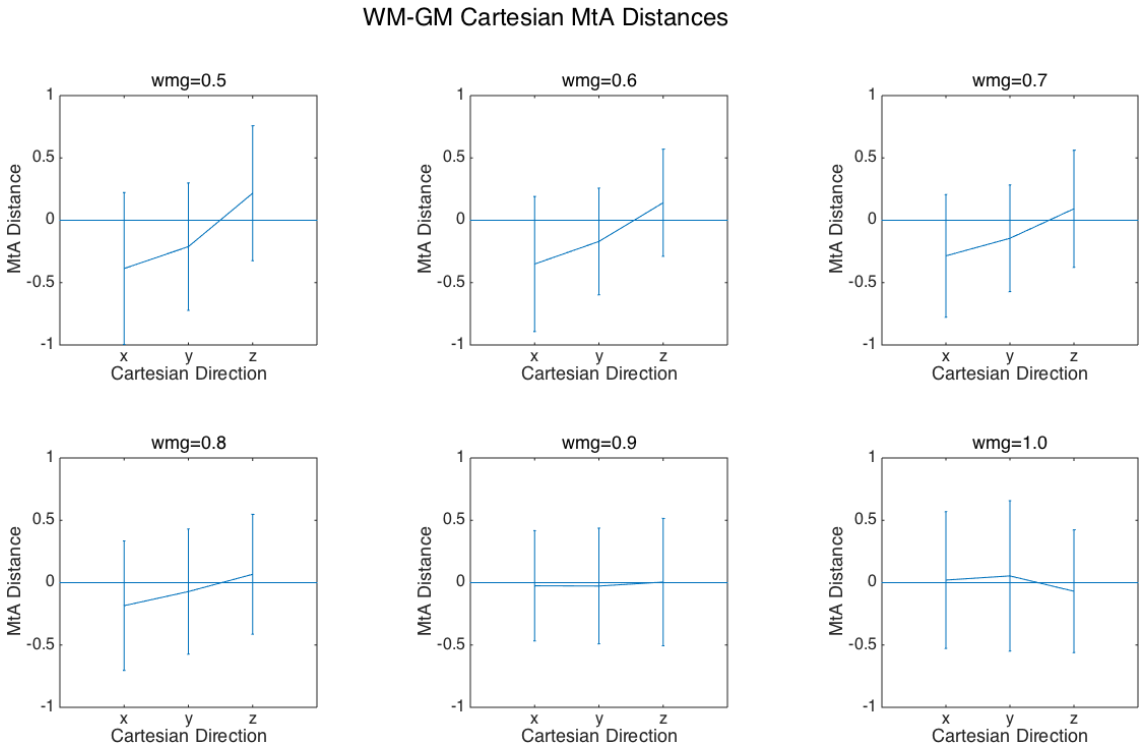

Figure 3.4.3.4 - Median distance in voxels in the x, y, and z directions from BrainVoyager generated WM-GM vertices to manually selected vertices using a spectrum of global white matter threshold values. Error bars show standard deviations.

It can be seen that for the optimized threshold (0.9), we see individual medians closer to zero than any other thresholds. While there are individual standard deviations smaller for some other thresholds, the incredibly accurate medians and relatively small standard deviations make 0.9 the dominant GMG threshold. Taking these optimization measures into account, a Global White Matter Threshold value of 0.9 was chosen for subsequent analyses.

3.4.4 Optimizing White Matter Local Threshold Values

The MtA optimization method was next used to optimize Local White Matter Threshold (WML) value, which was used subsequently to the Global White Matter threshold value to create white matter mask of the brain. BrainVoyager traces the borders defined by the global thresholding, and using smaller locally generated histograms, finds new peak values and uses the local threshold to include additional voxels in the white

matter mask. BrainVoyager uses a default value of 0.5 for this parameter (0.1 lower than the 0.6 used for the global threshold), providing a slightly more liberal inclusion of voxels on a smaller scale in regions determined more conservatively by the global thresholding.

Maintaining the previously determined Global White Matter Threshold of 0.9, and all other parameters with default values, grids were generated using local thresholds with values from 0.6 to 1.1. These grids were run through the MtA tool, with points manually selected from 31 evenly spaced planes through the region covered by BrainVoyager cortex grids. To demonstrate the MtA data for 6 grids we can graph the median MtA distances and their standard deviations for each grid.

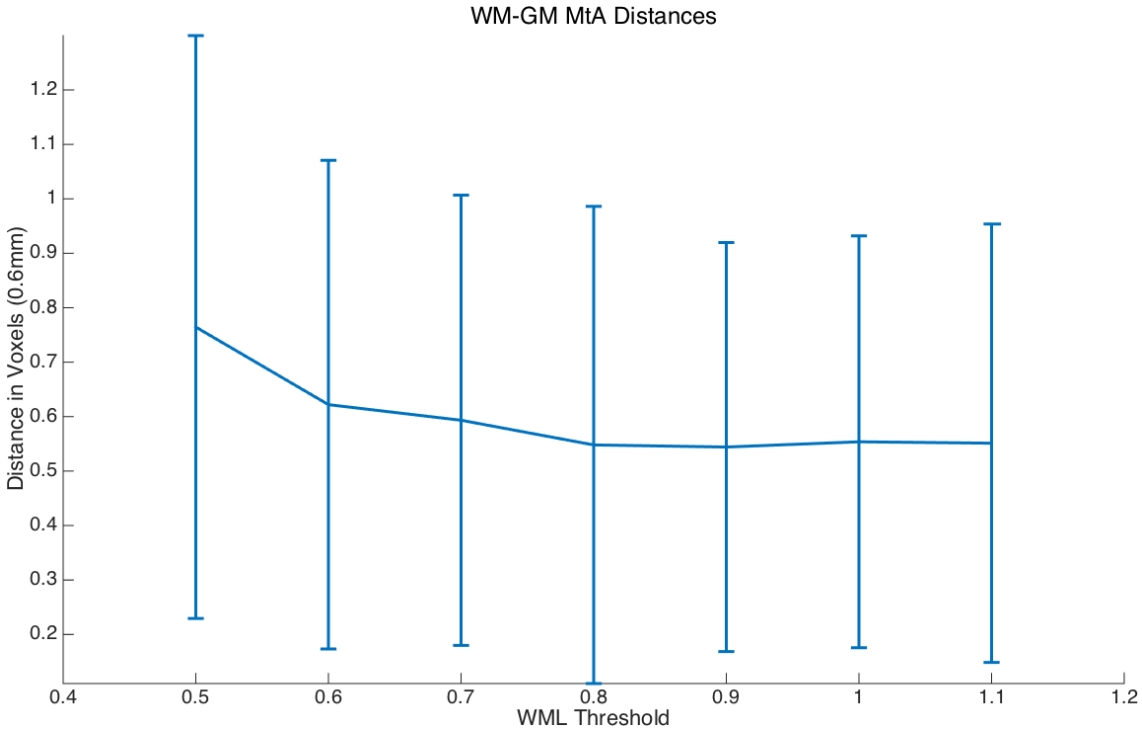

Figure 3.4.4.1 - Median distance in voxels from BrainVoyager generated WM-GM vertices to manually selected vertices using a spectrum of local white matter threshold values. Error bars show standard deviations.

Unlike the global threshold, we do not see a traditional optimization curve, with optimal values in the middle. This is due to the nature of the interaction between global threshold and local threshold. Any local threshold larger than our global threshold (0.9) is

unlikely to add more than a few voxels to the white matter mask, as it represents a more conservative threshold than that already used. A small number of voxels may be added as it is using a local histogram which may differ from the whole volume histogram, but not by a large amount. Therefore we see a plateau begin just after the global threshold.

By taking the rms of the median and standard deviation we can obtain an optimization measure for each.

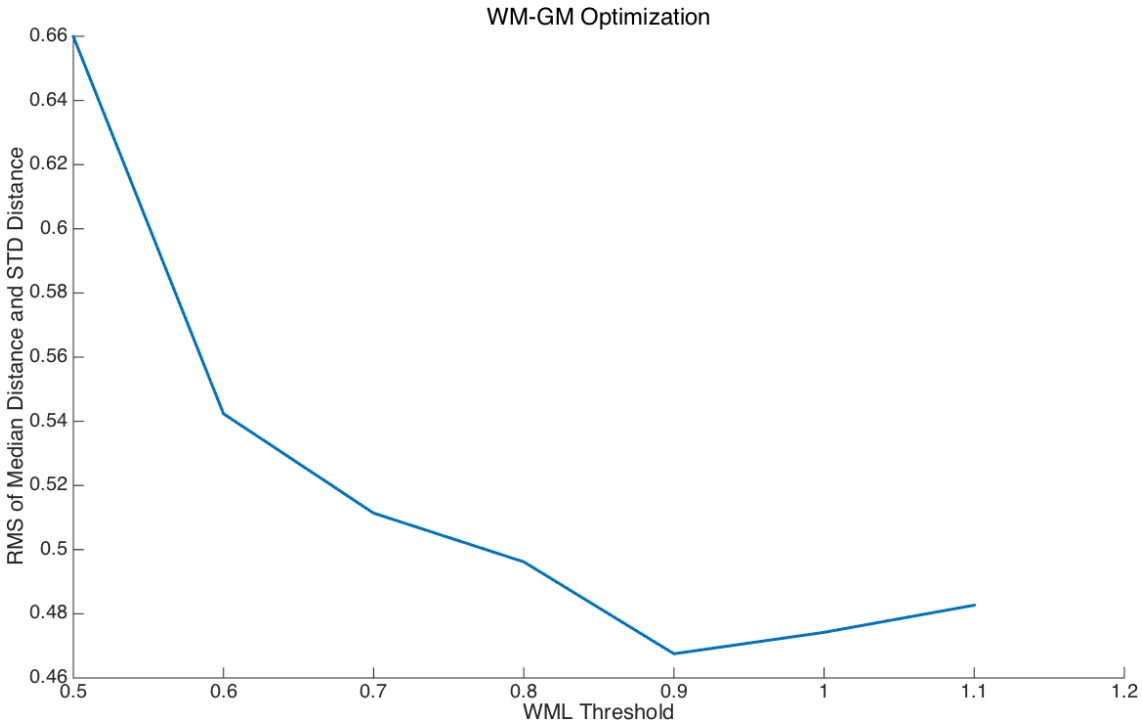

Figure 3.4.4.2 - WM-GM grid optimization measure using a spectrum of local white matter threshold values.

This graph shows, as could likely be predicted from figure 3.4.4.1, that a Global White Matter Threshold of 0.9 provides the most accurate results.

As done for the global threshold, we can examine the MtA distance values looking at each Cartesian direction.

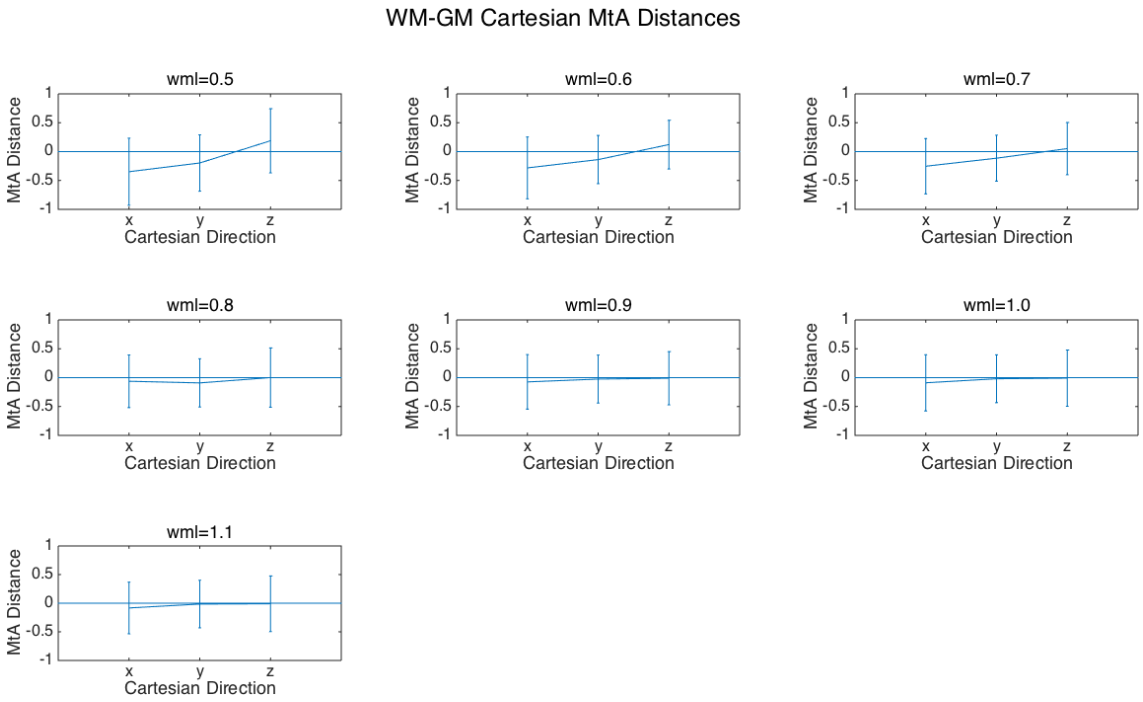

Figure 3.4.4.3 - Median distance in voxels in the x, y, and z directions from BrainVoyager generated WM-GM vertices to manually selected vertices using a spectrum of local white matter threshold values. Error bars show standard deviations.

This graph shows the increase in accuracy and decrease in variation leading up to a value of 0.9. It can also be seen that there is little variation in any individual direction past a threshold of 0.9.

3.4.5 Checking for Interaction in White Matter Thresholds

A concern in finding an optimal local threshold of 0.9 was that the local threshold was optimized using a global thresh of 0.9. To look at this a little more, a spectrum of global threshold values from 0.7 to 1.0 and local threshold values from 0.7 to 1.0 were all run with one another. The optimization values for all 16 resulting grids are plotted below.

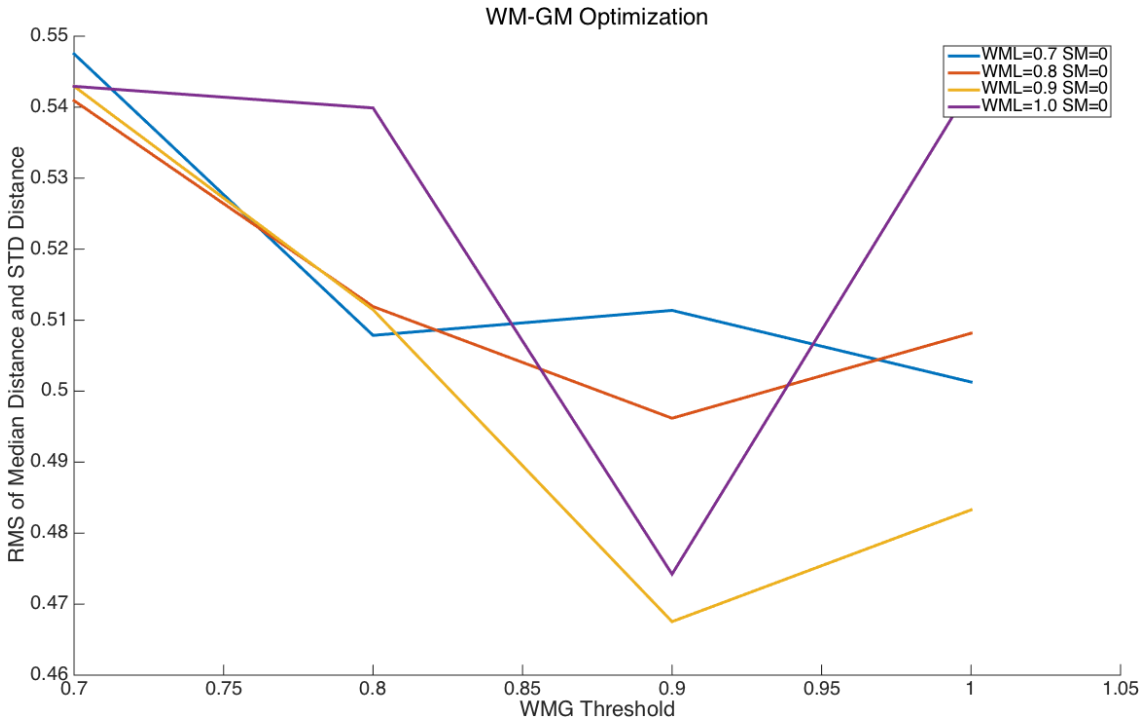

Figure 3.4.5.1 - WM-GM grid optimization measure using a spectrum of global (x-axis) and local (colored lines) white matter threshold values.

The apparent interaction between global and local thresholds can be explained as follows as follows. At a high global threshold some white matter voxels will be missed, and the lower local thresholds will find these voxels and add them to the mask. At lower global thresholds, the border will already be detected quite accurately, or with the inclusion of a few grey matter voxels. Here, high local thresholds which add few or no extra voxels will be best. The above graph realized this spectrum with some noise.

Importantly, at wmg=0.9, the optimization curve minimum can be seen in the local values with a local threshold of 0.7, 0.8, and 1.0 yielding worse results than 0.9. Thus, a Global White Matter threshold of 0.9 and a Local White Matter threshold of 0.9 were chosen.

3.4.6 Optimizing Global Grey Matter Values

The Grey Matter masking parameters were optimized next. The first parameter, while lacking detailed description in the documentation, is labeled as “Stop crit left from

GM peak", implying that it acts in a similar way to the WMG threshold to globally identify all grey matter voxels. The BV default for this value is 0.2. Grids were generated using values from 0 to 0.3 in steps of 0.05, and a fixed local grey matter threshold of 0. The resulting grids were run through the MtA tool.

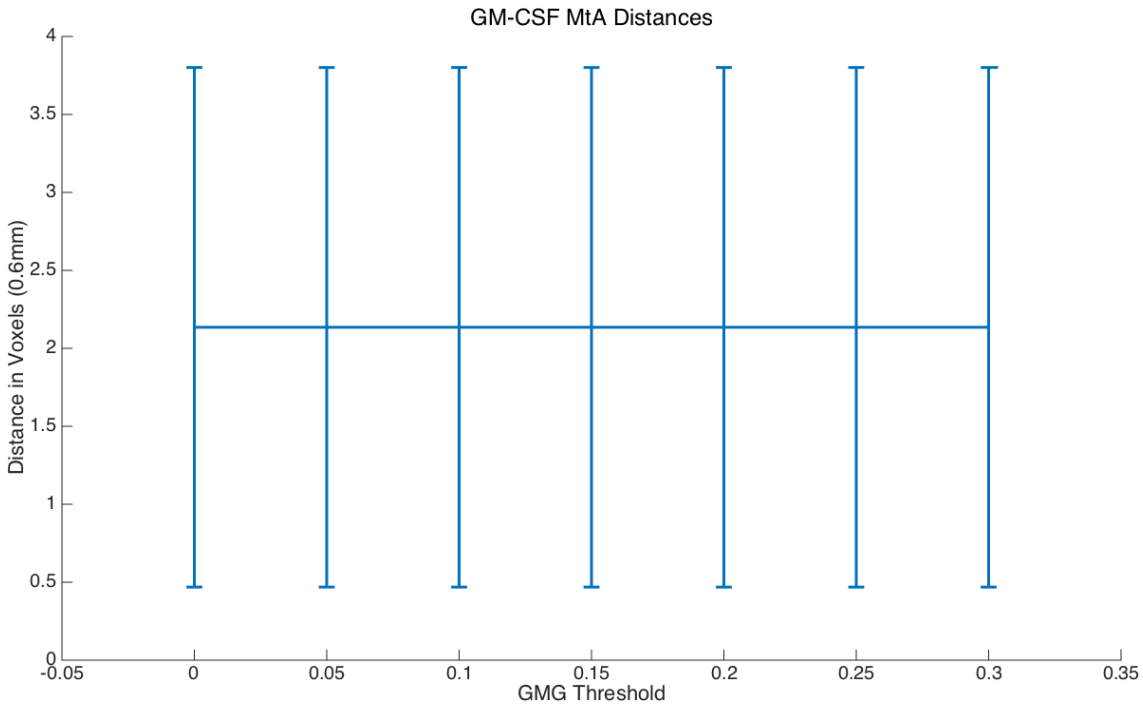

Figure 3.4.6.1 - Median distance in voxels from BrainVoyager generated GM-CSF vertices to manually selected vertices using a spectrum of global grey matter threshold values. Error bars show standard deviations.

Unexpectedly, the global grey matter threshold value was observed to have no effect. We see no change in MtA distance with this variable.

3.4.7 Optimizing Local Grey Matter Values

The second parameter, while lacking detailed description in the documentation, is labeled as "Local Stop Criterion", implying that it acts in a similar way to the WML threshold to identify additional grey matter voxels near the previously defined grey matter border. As there's a possibility that an interaction exists between the two parameters controlling the grey matter masking (and the GMG threshold does in fact

have an effect), we moved directly to a mixed optimization of a spectrum of both parameters. 12 grids were generated using global grey matter thresholds of 0, 0.15, and 0.3 and local grey matter thresholds of 0, 0.15, 0.30, and 0.45.

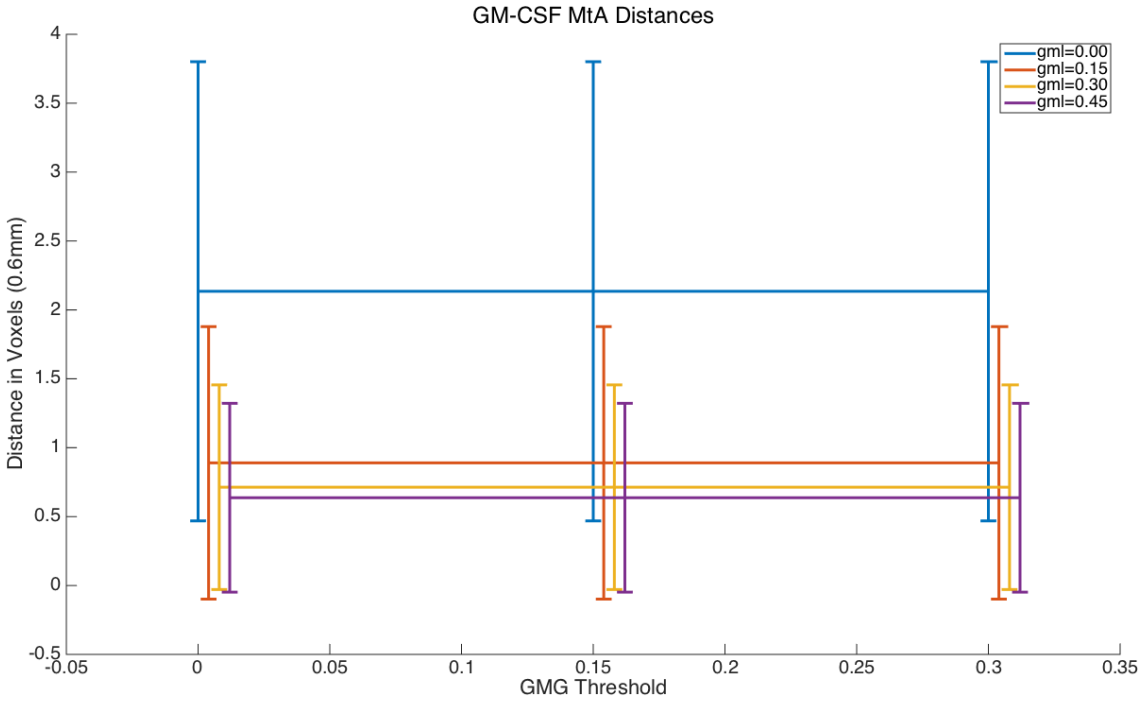

Figure 3.4.7.1 - Median distance in voxels from BrainVoyager generated GM-CSF vertices to manually selected vertices using a spectrum of global (x-axis) and local (colored lines) grey matter threshold values. Error bars show standard deviations.

The above figure confirms that the global grey matter threshold has no effect on MtA distance regardless of local grey matter threshold. We also see an improving MtA distance with increasing local grey matter threshold. To find an optimal local grey matter threshold, the range of values used was extended.

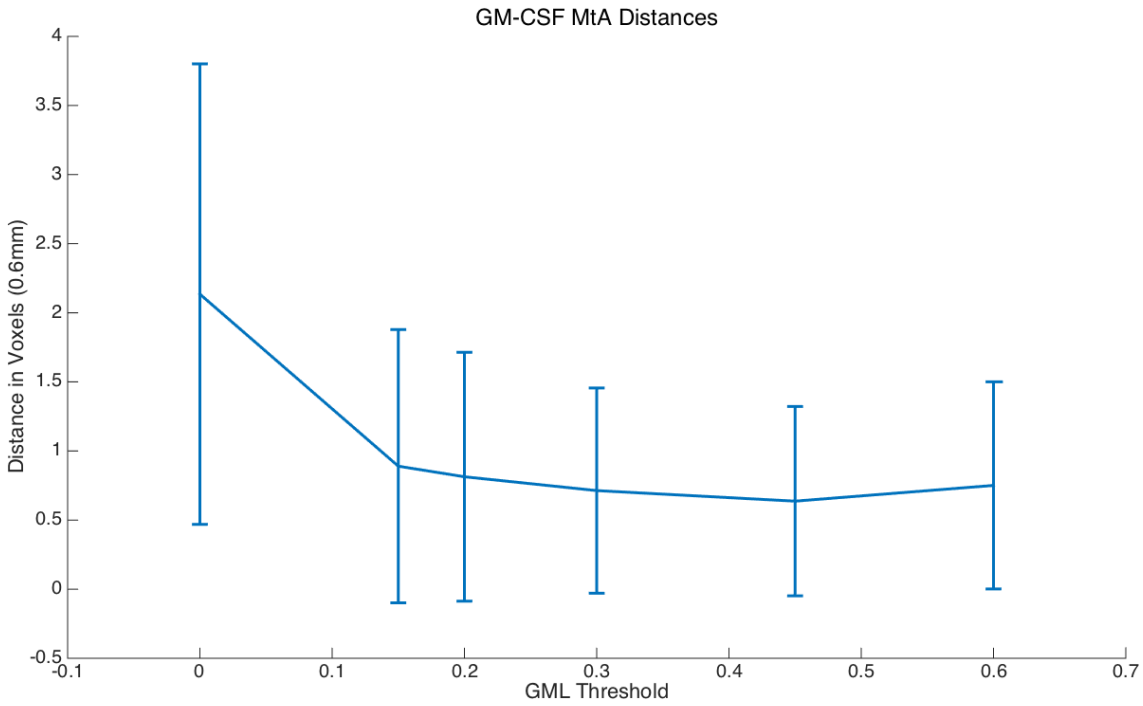

Figure 3.4.7.2 - Median distance in voxels from BrainVoyager generated GM-CSF vertices to manually selected vertices using a spectrum of local grey matter threshold values. Error bars show standard deviations.

Local grey matter thresholds between 0 and 0.6 (including the BrainVoyager default 0.2) were run. An optimization curve was obtained for which a local grey matter threshold of 0.45 returned the lowest MtA value, 22% lower than the default threshold.

3.4.8 Final BrainVoyager Input Values

Final user inputted BrainVoyager parameters are as follows:

Global White Matter Threshold = 0.9

Local White Matter Threshold = 0.9

Global Grey Matter Threshold = 0.45

Local Grey Matter Threshold = 0.45

These are the values found to optimize identification of white and grey matter voxels, and subsequent cortical laminae grid generation for the auditory region of our structural image.

It should be noted that there are a couple of additional optional steps and parameters (described below) that were examined in pilot work, but determined to not be necessary to optimize in this detail.

BrainVoyager recommends a sigma filter "enhance" step prior to mask generation. A mixed set of multiple WMG values and WML values were all created with and without the smoothing step. Results were systematically worse with the smoothing applied. Therefore it was not used in our pipeline.

The grey matter mask generation step also has a "number of dilation steps" parameter. Experimentation suggested that at its default value of 14, there were more than enough steps to reach the pial surface, and the thresholds alone did an excellent job defining this surface. This value would likely be more important in lower quality data where values beyond the grey matter might still be confused for grey matter and a hard stop is desired to prevent this.

3.5 Segmentation Outcome

3.5.1 Final Accuracy Measures

To compare to table 3.4.1.1, the following table provides a summary of all yielded MtA measurements using the final selection of BrainVoyager inputs.

Distance (Voxels)	Boundary	Median	Standard Deviation	Optimization
Absolute Distance	WM-GM	0.54	0.48	0.48
	GM-CSF	0.64	0.68	0.66

Unit Vector Distance (x/y/z)	WM-GM	-0.048 / -0.038 / -0.026	0.47 / 0.42 / 0.51	0.33
	GM-CSF	-0.25 / -0.13 / 0.087	0.70 / 0.57 / 0.58	0.45

Table 3.5.1.1 - Measures generated by the MtA tool to assess the accuracy of the BrainVoyager generated cortical maps using optimized parameters.

To emphasize the improvements granted by the MtA tool, the same table is shown with percent improvements from the default BrainVoyager Inputs to the optimized inputs.

Percentage Improvement	Boundary	Median	Standard Deviation	Optimization
Absolute Distance	WM-GM	28	6	25
	GM-CSF	19	19	20
Unit Vector Distance (x/y/z)	WM-GM	86 / 75 / 85	20 / 7 / -2	17
	GM-CSF	37 / 24 / 54	17 / 5 / 11	15

Table 3.5.1.2 - Percentage improvements in measures generated by the MtA tool to assess the accuracy of the BrainVoyager generated cortical maps between default and optimized parameters.

3.5.2 Pipeline Complications

Several observations were made while optimizing the pipeline related to the performance of certain BrainVoyager tools. A second participant was scanned, with only structural data being collected. This data was intended for evaluation of the segmentation pipeline. When this image was run through the brain extraction and intensity

homogeneity processing step, the remapping of peak grey and white histogram values to 100 and 160 was done incorrectly, instead mapping peak values to approximately 130 and 200. Although the documentation suggests that each step using histogram peak values recalculates histogram peak values, this was found to be incorrect. The white matter and grey matter identification tools were found to calculate their threshold values always relative to peak values of 100 and 160, even when these values did not correspond to the true histogram of the images. The cause of this remapping error was not determined, although the accuracy of brain extraction and the number of iterations of intensity inhomogeneity correction were observed to impact it when performing the work in 3.4.2. No combination of preprocessing was found to allow proper remapping, and the data could not be processed with BrainVoyager.

The actual histograms displayed by BrainVoyager also appear to be inaccurate. Histograms do appear to correspond to BrainVoyager documentation when calculated outside of BrainVoyager, but the histograms generated while using tools in the pipeline have incorrect range of values, and peak values relative to the image itself. Despite this, the values BrainVoyager pulls from the image are correct, and do not match the incorrect histogram.

Our final recommendations when using this BrainVoyager pipeline are to pay special attention to the remapping of values in the first steps, and to optimize user inputted parameters specific to the region of interest. It is likely based on our experience with a second subject that optimal parameters will vary between subjects.

3.6 References

1. Balafar, M. a., Ramli, a. R., Saripan, M. I., & Mashohor, S. (2010). Review of brain MRI image segmentation methods. Artificial Intelligence Review, 33(3), 261–274. doi:10.1007/s10462-010-9155-0
2. Gudbjartsson, H., & Patz, S. (1995). The Rician Distribution of Noisy MRI Data Hákon. Magnetic Resonance in Medicine, 34(6), 910–914.

3. Krüger, G., & Glover, G. H. (2001). Physiological noise in oxygenation-sensitive magnetic resonance imaging. Magnetic Resonance in Medicine, 46(4), 631–637. doi:10.1002/mrm.1240
4. T, I. D., Goossens, B., & Philips, W. (2015). MRI Segmentation of the Human Brain : Challenges , Methods , and Applications, 2015.
5. De Martino, F., Schmitter, S., Moerel, M., Tian, J., Ugurbil, K., Formisano, E., … de Moortele, P.-F. Van. (2012). Spin echo functional MRI in bilateral auditory cortices at 7 T: an application of B_1 shimming. NeuroImage, 63(3), 1313–20. doi:10.1016/j.neuroimage.2012.08.029
6. Sled, J., Zijdenbos, a, & Evans, a C. (1997). A comparison of retrospective intensity non-uniformity correction methods for MRI. In Information Processing in Medical Imaging, 459–464. doi:10.1007/3-540-63046-5_43
7. Lüsebrink, F., Wollrab, A., & Speck, O. (2013). Cortical thickness determination of the human brain using high resolution 3T and 7T MRI data. NeuroImage, 70, 122–131. doi:10.1016/j.neuroimage.2012.12.016
8. Ress, D., Glover, G. H., Liu, J., & Wandell, B. (2007). Laminar profiles of functional activity in the human brain. NeuroImage, 34(1), 74–84. doi:10.1016/j.neuroimage.2006.08.020
9. Olman, C. a, Harel, N., Feinberg, D. a, He, S., Zhang, P., Ugurbil, K., & Yacoub, E. (2012). Layer-specific fMRI reflects different neuronal computations at different depths in human V1. PloS One, 7(3), e32536. doi:10.1371/journal.pone.0032536
10. Waehnert, M. D., Dinse, J., Weiss, M., Streicher, M. N., Waehnert, P., Geyer, S., … Bazin, P. L. (2013). Anatomically motivated modeling of cortical laminae. NeuroImage, 93, 210–220. doi:10.1016/j.neuroimage.2013.03.078
11. Huber, L., Goense, J., Kennerley, A. J., Trampel, R., Guidi, M., Reimer, E., … Möller, H. E. (2014). Cortical lamina-dependent blood volume changes in human brain at 7T. NeuroImage, 107, 23–33. doi:10.1016/j.neuroimage.2014.11.046
12. De Martino, F., Moerel, M., Xu, J., van de Moortele, P.-F., Ugurbil, K., Goebel, R., … Formisano, E. (2014). High-Resolution Mapping of Myeloarchitecture In

Vivo: Localization of Auditory Areas in the Human Brain. Cerebral Cortex (New York, N.Y. : 1991). doi:10.1093/cercor/bhu150

13. Kemper, V. G., De Martino, F., Vu, A. T., Poser, B. a., Feinberg, D. a., Goebel, R., & Yacoub, E. (2015). Sub-millimeter T2 weighted fMRI at 7 T: comparison of 3D-GRASE and 2D SE-EPI. Frontiers in Neuroscience, 9(May), 1–14. doi:10.3389/fnins.2015.00163
14. De Martino, F., Zimmermann, J., Muckli, L., Ugurbil, K., Yacoub, E., & Goebel, R. (2013). Cortical depth dependent functional responses in humans at 7T: improved specificity with 3D GRASE. PloS One, 8(3), e60514. doi:10.1371/journal.pone.0060514
15. Cusack, R., Vicente-Grabovetsky, A., Mitchell, D. J., Wild, C. J., Auer, T., Linke, A. C., & Peelle, J. E. (2015). Automatic analysis (aa): efficient neuroimaging workflows and parallel processing using Matlab and XML. Frontiers in Neuroinformatics, 8(January), 1–13. doi:10.3389/fninf.2014.00090
16. Jones, S. E., Buchbinder, B. R., & Aharon, I. (2000). Three-Dimensional Mapping of Cortical Thickness Using Laplace ’ s Equation. Human Brain Mapping, 11, 12–32.

Figure 3.1.3.1 - Reprinted from NeuroImage, Volume 70, Falk Lüsebrink, Astrid Wollrab, Oliver Speck, Cortical thickness determination of the human brain using high resolution 3 T and 7 T MRI data, Pages 122–131, 2012, with permission from Elsevier.

4 Chapter 4: Functional Results

An analysis pipeline was created to process the functional data. We then required a method of integrating the results of this, which were voxels in a volume, with the meshes that came from segmentation. This chapter first outlines the functional analysis pipeline, including an explanation of the module written to integrate the BrainVoyager cortical laminae meshes in a resampling process. It will then look at functional activation maps in the form of 3D rendered contrast maps, and finally discuss the findings, and possible future directions.

4.1 Analysis Pipeline

Functional analysis for this project was completed using SPM8 and Automatic Analysis (aa) [1]. *aa* is a framework for MRI analysis that allows for efficient workflow. It allows for thorough tracking and repetition of complicated pipelines without the need for tedious manual analyses.

4.1.1 Raw Data Conversion

Functional data from the scanner is provided in 4D NIfTI files; a single file for each timecourse of functional scans. These 4D files are first split into a single NIfTI file for each 3D volume in the timecourse. This was the format *aa* modules were written to expect (although since this project began, support for 4D files has been incorporated into aa).

4.1.2 Slice Timing Correction

As our functional data were collected using a 2D EPI sequence, slices are acquired sequentially, distributed throughout our 2 second TR. The BOLD signal for different slices was therefore sampled at slightly different times. SPM's slice timing correction takes into account the slice acquisition order (Interleaved) and a chosen reference slice (slice 1), interpolating the time-course for each voxel in time to match all voxels across each volume in time.

4.1.3 Image Realignment

To compensate for subject movement during the scan, SPM's realign function estimates, for each time series volume, the rigid body movement parameters in three translational axes and three rotational axes required to align each volume with the first in the series. These alignment parameters are updates in each volume's header, but we do not reslice (resample and interpolate the volumes so each voxel in each volume represents the same point in real space) the EPI volumes as one normally might in this type of analysis. This is because later, in our laminar resampling step, we will sample and interpolate these volumes using structurally derived coordinates. By leaving them in their original space, some volumes will have data coordinates closer to some of our sampling coordinates (by nature of the slight subject movements over time), and we will gain some degree of super-resolution.

The realignment module also creates a mean EPI volume for the first EPI session. This is used in later steps, and is helpful for visualization of the functional volumes.

4.1.4 EPI Undistortion

We evaluated an EPI undistortion module written for automatic analysis (aa) [2]. This module requires both a phase and magnitude image from the field mapping sequence. The phase image was processed by a robust 3D phase unwrapping algorithm [3]. The magnitude image was fed to a brain extraction tool (BET) to create a brain mask. The masked phase data were dilated and smoothed, and the sequence parameters are used to calculate a forward distortion map, which can be used to remove distortions from each EPI volume. This module was not applied in the final pipeline as it was deemed unnecessary (as explained in 3.1.4).

4.1.5 Image Coregistration

To make associations between the structural and functional images, we must first ensure they are properly aligned with one another. The SPM coregistration function co-registers the structural image to the mean EPI image by optimizing a rigid-body transformation to minimize an objective function from information theory, mutual

information. The structural alignment parameters were updated, and the EPI's weren't changed.

4.1.6 Laminar Resampling

A custom *aa* module was written to perform the resampling necessary for the laminar analysis, based around SPM's resampling function. The module operates on a one-instance-per-session level, running once for each session and for each subject. It is passed, as inputs, the functional images, the structural images, the BrainVoyager generated cortical maps, and a smoothing parameter.

The module begins by parsing the BrainVoyager text output and reformatting the vertices into usable matrices.

The module then loads the structural image and, using SPM's resampling function and the list of vertices from BrainVoyager, creates a resampled structural volume in "BV space". This volume is the width and length of the grid size, and as deep as the number of grids generated, each plane representing the flattened surface of one cortical depth grid. This volume is written to file.

The module then loops over the number of EPI volumes. For each, it loads the volume and, using the alignment parameters from this EPI and the alignment parameters from the structural volume, calculates the transformation matrix to convert coordinates from structural space to EPI space. It then uses this transformation matrix to convert the BrainVoyager vertices from structural space to EPI space. Then, looping over the number of BrainVoyager grids, it resamples the EPI volume with the transformed vertices and performs 2D Gaussian smoothing (FWHM=2 voxels) over the sampled surface. It then combines these resampled and smoothed surfaces into one 3D volume in "BV space", and writes it to file.

The module then creates a resampled mean EPI volume in "BV space" in the same way as previously described for the structural, except using the transformed BrainVoyager vertices in EPI space.

Lastly, using the structural volume, and mean EPI volume, it creates two “vertex maps”, with the vertices from all of the BrainVoyager grids indicated in white atop the standard volume. These are written to file. This allows for easy confirmation that the transformation is occurring correctly and that the coregistration is adequate for properly resampling the intended grey matter of the EPI volumes.

4.1.7 Modeling

A modelling module was used to perform conventional univariate analysis. Each combination of the two conditions (low and high frequency), and two tasks (change detection and imagery) were modeled separately, along with the maintenance period and intertrial interval. A contrast module was used to produce a variety of contrast maps.

4.2 Visualization of Functional Activation

To visualize the functional results, the vertices generated by BrainVoyager were used to create 3D renders of each layer, onto which the contrast maps were visualized. Below is an example of a single rendered grid to provide a frame of reference for looking at the subsequent renders. It is important to note that our subject presents with a split Heschl's Gyrus in the hemisphere acquired (the right). The primary gyrus is labelled HG1 and the smaller secondary gyrus is labelled HG2 in the figure below.

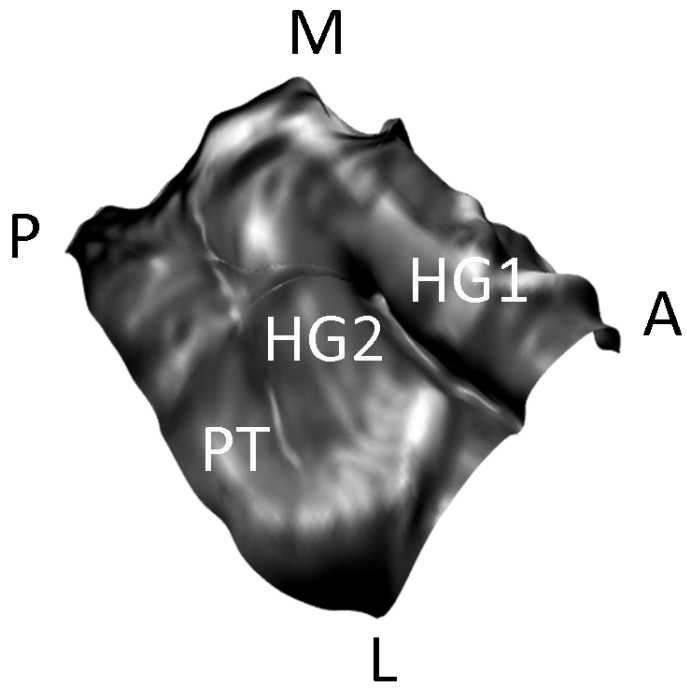

Figure 4.2.0.1 - An example of a rendered cortical layer grid. Directions are indicated by the black text (A - anterior, P - posterior, M - medial, L - lateral). Important structures are indicated by the white text (HG1 - Heschl's gyrus, HG2 - Heschl's Gyrus, PT - Planum Temporale).

4.2.1 Contrast Maps

The first activation we wanted to look for was a simple sound against ITI contrast, to show that we could detect auditory activation. This contrasted activity present during the first and second sound of both tasks and both conditions against the ITI of both tasks and both conditions. Figure 4.2.1.1 shows that activation was present in all auditory layers with more activation in the superficial layers near the pial surface. Much of that activity lay on or between the two Heschl's gyri where we would expect AI to be located. As well we can see spatially distinct activation across layers, for example the large active region on posteromedial HG2 at the pial surface appears to shift towards HG1 in the middle layers, and disappear in the deep layers.

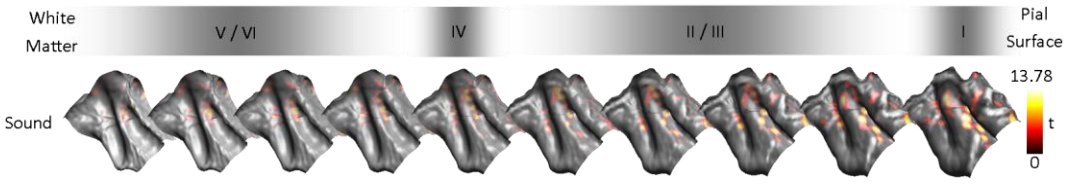

Figure 4.2.1.1 - Activation by layer maps for a contrast of all sounds against all maintenance intervals.

A previous study [4] of a similar auditory stimulation paradigm (change detection) showed a suppression of activity in auditory cortex during the maintenance period of the task. Two hypotheses were put forwards by these authors. One was that this suppression was in the same neurons that encoded the stimulus, and it protects short-term memory representations from being replaced by the encoding of new sounds. Another was that there is a centre-surround patch of inhibition, so that the remembered frequency is actually positively activated during the maintenance period, but it suppresses neurons representing neighboring frequencies. However, at the coarse scale of the voxels in [4] (2.4 mm isotropic, with 10 mm FWHM 3D smoothing) only a patch of inhibition is seen. It is possible that the higher resolution in our study will distinguish this. We therefore performed a negative maintenance contrast, searching for suppression during the maintenance periods of both tasks and both conditions. Figure 4.2.1.2 shows suppression during the maintenance period across middle and shallow layers. The suppression residing along HG2 overlaps with activation during the sound portion of the task as reported by Linke et al. [4]. No excitatory voxels were seen: the positive maintenance contrast was blank, and even at the higher resolution of our study no support was found for the centre-surround hypothesis.

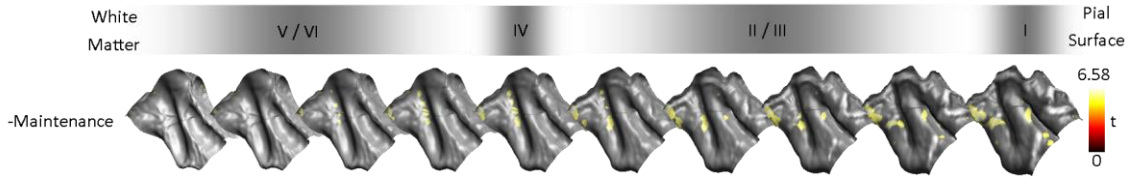

Figure 4.2.1.2 - Suppression by layer maps for a contrast of negative maintenance against the ITI.

In a subsequent study, Linke et al. [5] found that while there was suppression during the maintenance period of a change detection task, the maintenance period during an imagery task showed positive activation in the same regions as during the sound phase. We first performed contrasts looking for activation during the maintenance period of either task but found no activated regions. We therefore performed negative maintenance contrasts for imagery and change detection against ITI separately, as well as contrast of the maintenance period of one task against the other. Figure 4.2.1.3 shows suppression during the imagery task in a similar pattern to the above suppression shown for all maintenance periods, but very little suppression during the change detection task. Contrasts of the maintenance periods of each task against each other showed no activity or suppression unique to either task.

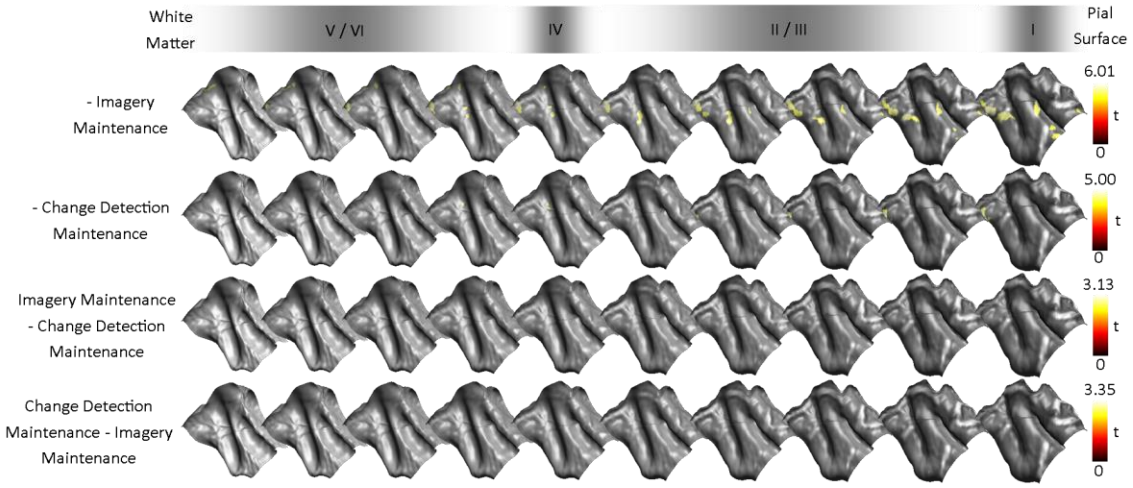

Figure 4.2.1.3 - Activation by layer maps for a contrast of sound against ITI for the imagery and change detection tasks separately.

Next, we examined differences in activation between the key conditions of interest. For the low- and high- frequency stimuli separately, we contrasted activation evoked by sound against the ITI. Figure 4.2.1.4 shows areas activated by high- and low-frequency sounds. While both conditions elicited activity in similar areas across all layers, certain regions of activation (e.g. the active regions on posteromedial HG2) appear to show spatial shifts in activation, suggesting detection of tonotopic gradients. As with the first sound contrast, we see spatially distinct activation patterns across layers for the low and high frequency conditions.

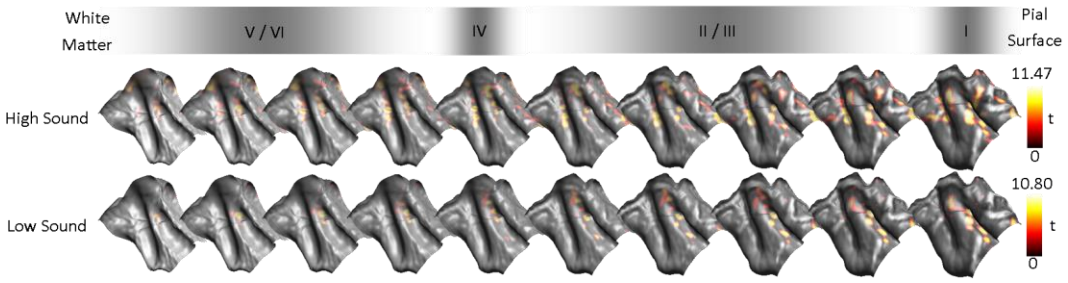

Figure 4.2.1.4 - Activation by layer maps for a contrast of sounds against ITI for the high frequency and low frequency conditions separately.

To evaluate the consistency of these responses, we ran contrasts of the low frequency and high frequency sounds against ITI separately for the imagery and change detection tasks. Even for these entirely independent datasets, Figure 4.2.1.5 shows that there was a remarkable degree of consistency in the layer-specific patterns of activation across the replications. Specifically, the "Low CD" and "Low IM" contrasts evoked very similar activation patterns, while the "High CD" and "High IM" contrasts evoked very similar patterns that were both distinct from the low frequency contrasts.

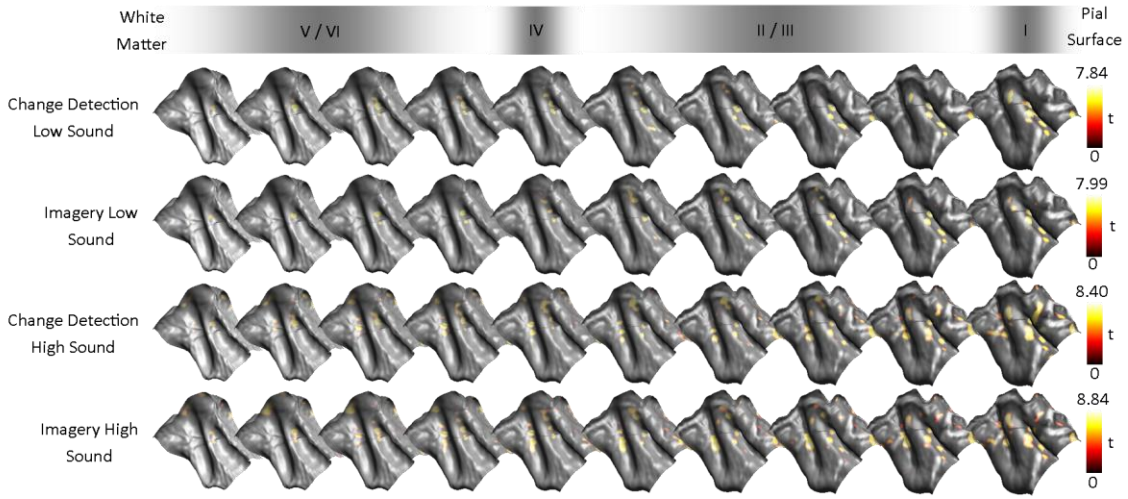

Figure 4.2.1.5 - Activation by layer maps for a contrast of sounds against ITI for the high frequency and low frequency conditions, and imagery and change detection, separately.

To evaluate the significance of the spatial shift between low- and high- frequency sounds we ran contrasts of high-frequency sound against low-frequency sound and vice versa. Figure 4.2.1.6 shows that while the activation due to high frequency sounds does

cover some areas (medial HG1, and PT) which aren't evoked by the low frequency sounds, the low frequency sounds do not evoke activation significantly stronger than the high frequency sounds in any region. This implies that the low frequency sounds may be activating a subset of regions that the high frequency sounds activate, and we cannot claim there are specific regions that activate preferentially each condition.

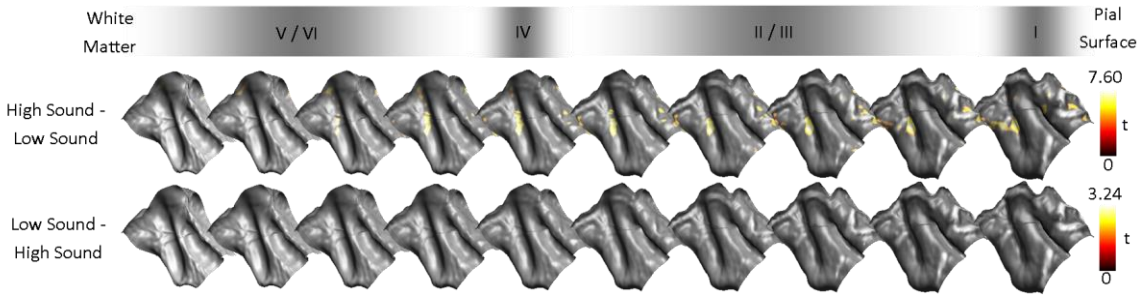

Figure 4.2.1.6 – Activation by layer maps for a contrast of high frequency sound against low frequency sound, and of low frequency sound against high frequency sound.

Lastly, we wanted to look for a difference in activation between the imagery and change detection tasks. We ran independent sound against ITI contrasts for the two tasks. Figure 4.2.1.7 shows very similar activation patterns between the two with very similar overall activation levels, and only small spatial shifts in activation locations.

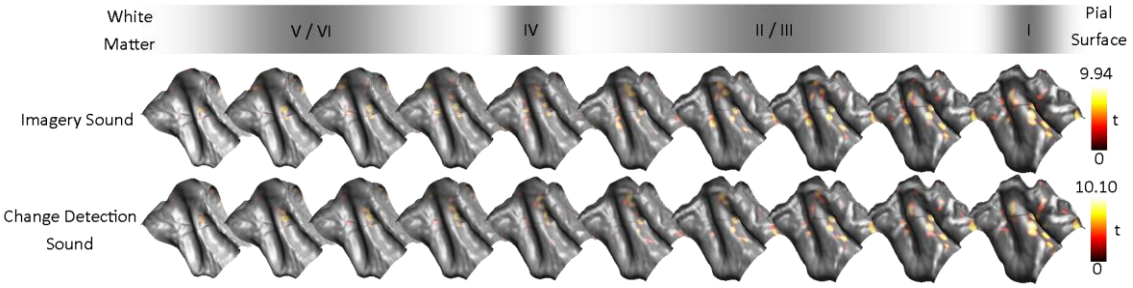

Figure 4.2.1.7 - Activation by layer maps for a contrast of sound against ITI for the imagery and change detection tasks separately.

4.3 Discussion

The responses observed to sound validated the protocol choices in Chapter 2. Extensive activation was found in the regions of auditory cortex where auditory activation would be most expected (Heschl's gyrus and nearby cortex). Furthermore, evidence was found of different activation patterns across layers between the white matter and pial surface boundaries. This has exciting potential for future neuroscientific studies. It is important to remember that the BrainVoyager grids were vertex matched. That is, vertex (x_i,y_i) came from the same cortical column across layers. This means that the shifting spatial location of activation was not due to an improper alignment of cortical sampling grids, but to locally spatially varying activation in the cortex.

We found suppression in auditory regions during the maintenance period, mirroring the findings of Linke et al [4]. Furthermore, even at the high resolution of our data, suppression during the maintenance period was found in the same regions as activation to sound during the task. This suggests that its cause is suppression of the same neurons involved in perception, rather than a centre-surround suppression effect. Interestingly the spatial correlation between these patterns appears strongest in the middle and deep layers, with good spatial overlap in activation/suppression while there is slightly more variability in shallow layers. This could possibly indicate suppression in layer IV, the thalamorecipient layer, where suppression of sound would have the greatest effect.

When probing for task specific activity or suppression during the maintenance period of the task, we were unable to show activation during the imagery maintenance as reported in Linke et al 2015 [5]. Given that signal in the maintenance period, is harder to detect than positive activation due to the presentation of sound, it is possible that the lack of evidence here stems from a lack of power. This is also data from a single subject, whereas Linke et al reported group data in twenty-five subjects. Data collection in more subjects is needed to make more robust conclusions in this area.

For both high and low frequency conditions, highly similar activation patterns were seen when comparing sound presentation in the replications in the imagery and change detection tasks. These tasks represent completely independent sets of data, and

reveal remarkable consistency in 7T functional activation patterns even at high resolution.

Contrasts of high- and low- frequency sounds against one another indicated only that regions activated by low frequency sounds may be a subset of regions activated by high frequency sounds. However, there are some spatial shifts in the exact location of regions activated by the two conditions visible on the contrast of each against the ITI. Although difficult to resolve by eye in the figure, there is a trend in the direction of shift the activated regions from lateral to medial from high to low frequencies. This is evident in all of the activation on HG2. Furthermore, the activation for high frequencies is nearly evenly distributed across HG1, HG2, and PT, while activation for low frequencies is more isolated to HG2 and the sulcus between the two Heschl's gyri. This is consistent with previous mappings of tonotopic gradients which show low frequency preference along Heschl's gyrus, and high frequency preference extending away from it anteromedially and posterolaterally [6].

We theorized that the imagery task, being an inherently top-down process involving higher order areas of the brain, would increase input to superficial layers of the brain and increase activation in layers other than layer IV. Figure 4.2.1.5 shows a comparison of activation between the imagery and change detection tasks collapsed across conditions. We saw very similar overall patterns of activation. The two tasks shared activation in most regions, with small shifts in some activations, and some small additional regions of activation for both tasks. Overall degree of activation did not seem to differ between the tasks across layers. It is possible that this is due to a task order effect. As our data came from a single subject across several scan sessions (with both tasks occurring in every session), it is possible that a similar "rehearsal strategy" as employed in the imagery task became utilized in the change detection task as well. Performing all change detection blocks before imagery blocks might help minimize this.

4.4 Conclusions

With reference to our earlier stated goals we:

1. Obtained high resolution structural and functional data in auditory cortex at 7T utilizing the protocols described in Chapter 2.
2. Created and optimized a segmentation pipeline for specifying the locations of cortical laminae by depth using BrainVoyager and the methods and tools described in Chapter 3.
3. Created a pipeline for analysing the functional data as a function of cortical depth, using *aa* and a custom resampling module described in section 4.1.
4. Identified functional activation differences at varying cortical depths, as demonstrated by the results presented in section 4.2.

We were able to differentiate spatially varying activation to sound across depths of auditory cortex. We found previously described suppression in auditory cortex during a memory maintenance period, with good spatial correlation to sound activation. We detected spatial shifts in activation between high and low frequency sounds, in agreement with previously described tonotopic gradients. We did not see evidence for laminar activation differences between change detection and imagery tasks.

4.5 Future Directions

This work represents an early validation of methods for laminar imaging of auditory cortex. Possible improvements and next steps will be covered by chapter.

4.5.1 Future Protocols

The protocols used in this study allowed us to achieve our objectives, but alterations would allow for slightly different types of studies. In all of our results we saw a bias in activation levels towards the pial surface, similar to what has been previously documented with regards to GE-EPI sequences. With this bias in place, we were limited to making laminar specific claims based on comparisons between contrasts. If adequate sensitivity could be achieved with other, more spatially sensitive sequences (SE-EPI or 3D-GRACE) it might be possible to make laminar claims based on absolute activation in single contrasts.

Also, our protocols' FOV allowed for the collection of nearly an entire hemisphere of data. This was excellent for the early stages of this project, where signal localization was required, and the analysis stages, where alignment of volumes would be much more difficult with a smaller FOV. For future studies with singular premeditated focus, FOV might be sacrificed to gain an even higher functional resolution, allowing further distinction of activation by depth, perhaps with confidence down to the level of individual layers.

Alternate methods might also be used in tandem. Incredibly detailed work was recently done in rats with line-scanning fMRI [7] that might be replicated in humans which might give insight into why we see the laminar differences we do in this study. As well, very interesting work matching the BOLD signal to neuronal activity using combines 7T fMRI and ECoG has been done at a fine, but not laminar scale [8]. Extension of this work using laminar fMRI would validate the source of the BOLD signal at a laminar level.

4.5.2 Segmentation possibilities

The segmentation pipeline developed using BrainVoyager and optimized with custom MATLAB tools produced precise cortical laminar grids used in this project. This method is limited to a small subsection of cortex as a trade-off for the grids regularity and vertex correspondence. These are very important for assessing laminar differences. If these principles could be maintained while segmenting the entire hemisphere, laminar differences across brain regions could be compared. However, our optimization work showed that optimal segmentation parameters for one brain region often performed poorly in others. This might be solved with improved inhomogeneity correction methods, or alternate thresholding approaches. The current methods, fortunately, are perfectly suited to the single region approach our project required.

The BrainVoyager tools are built to work with T1-weighted anatomical images. With ultra-high-field fMRI however, the mean images obtained from our EPI sequences might have sharply enough delineable boundaries for segmentation to be performed directly on them. This would eliminate the error possibly introduced in the transformation

from structural to functional coordinates due to image coregistration or EPI distortion. Although our project found these problems to not be significant or require special attention to deal with, other studies and other sequences might struggle more to correct for these.

4.5.3 Next steps for understanding auditory processing

Our project chose two dimensions on which to examine laminar auditory processing. We differentiated stimuli based on low and high frequency to look for topographical representations, and used tasks with different levels of cognitive effort to control input to different cortical layers. While we were able to see some small sensible shift in activation between low and high frequencies, a task with a greater range of frequencies should be able to produce a more detailed best frequency map. This would allow better visualization of tonotopic gradients, possibly allowing differences between layers to be identified. Our two tasks didn't seem to generate different levels of activation at any layer. This might be due to the way subjects approach the two tasks and the order they're completed in. It might also be that the differences do exist, but they're masked by a GE-BOLD pial surface bias. Controlling for either of these possibilities in future work will be telling.

4.6 References

1. Cusack, R., Vicente-Grabovetsky, A., Mitchell, D. J., Wild, C. J., Auer, T., Linke, A. C., & Peelle, J. E. (2015). Automatic analysis (aa): efficient neuroimaging workflows and parallel processing using Matlab and XML. Frontiers in Neuroinformatics, 8(January), 1–13. doi:10.3389/fninf.2014.00090
2. Cusack, R., Brett, M., & Osswald, K. (2003). An evaluation of the use of magnetic field maps to undistort echo-planar images. NeuroImage, 18(1), 127–142. http://doi.org/10.1006/nimg.2002.1281
3. Cusack, R., & Papadakis, N. (2002). New robust 3-D phase unwrapping algorithms: application to magnetic field mapping and undistorting echoplanar images. NeuroImage, 16(3 Pt 1), 754–764. http://doi.org/10.1006/nimg.2002.1092

4. Linke, A. C., Vicente-Grabovetsky, A., & Cusack, R. (2011). Stimulus-specific suppression preserves information in auditory short-term memory. Proceedings of the National Academy of Sciences of the United States of America, 2–7. doi:10.1073/pnas.1102118108
5. Linke, A. C., & Cusack, R. (2015). Flexible information coding in human auditory cortex during perception, imagery, and STM of complex sounds. *Journal of Cognitive Neuroscience*, *7*(27), 1322–1333. doi:10.1162/jocn_a_00780
6. Moerel, M., De Martino, F., & Formisano, E. (2014). An anatomical and functional topography of human auditory cortical areas. Frontiers in Neuroscience, 8(8 JUL), 1–14. doi:10.3389/fnins.2014.00225
7. Yu, X., Qian, C., Chen, D., Dodd, S. J., & Koretsky, A. P. (2014). Deciphering laminar-specific neural inputs with line-scanning fMRI. Nature Methods, 11(1), 55–8. doi:10.1038/nmeth.2730
8. Siero, J. C. W., Hermes, D., Hoogduin, H., Luijten, P. R., Ramsey, N. F., & Petridou, N. (2014). BOLD matches neuronal activity at the mm scale: A combined 7T fMRI and ECoG study in human sensorimotor cortex. NeuroImage, 101, 177–184. doi:10.1016/j.neuroimage.2014.07.002

Curriculum Vitae

Name:	Jacob Matthews
Post-secondary Education and Degrees:	University of Western Ontario London, Ontario, Canada 2009-2013 BMSc Medical Biophysics
Honours and Awards:	The Maurice and Myrtle Reinhart Scholarship for honesty and integrity in the pursuit of high achievement (Competitive Cash Award) The Marceline Allendorf Gibson Scholarship (Competitive Cash Award)
Related Work Experience	Graduate Teaching Assistant University of Western Ontario 2013-2015 Research Assistant Cusack Lab, BMI, UWO 2013
Volunteer Activities	Dental Assistant, Speroway – Accompanied a team of approximately 40 Physicians, Dentists, and assorted Medical Assistants on Medical/Dental aid trip to El Salvador. Primarily worked as first assistant with one of the team's Dentists, assisting in extraction and filling procedures. Also assisted with the Pharmacy team, and administrative organization. In our five field days, the team assisted just under 6000 local people; a record for Speroway.

Publications:

Linke A, Matthews J, Wild C, Cusack R. (2014). Multiband-EPI acquisitions preserve BOLD SNR in the presence of head motion. NeuroImage. Submitted

Linke A, Matthews J, Gati J, Cusack R. (2013). Using high-field fMRI and multivariate methods to study neural representations of complex sounds in human auditory cortex. Association for Research in Otolaryngology MidWinter Meeting, Baltimore, United States, 2013-02-16, Invited Talk, Published Abstract